JACS
JOURNAL OF THE AMERICAN CHEMICAL SOCIETY
pubs.acs.org/JACS
Article

Factors Governing Oxygen Vacancy Formation in Oxide Perovskites

Robert B. Wexler, Gopalakrishnan Sai Gautam, Ellen B. Stechel, and Emily A. Carter*

Cite This: J. Am. Chem. Soc. 2021, 143, 13212−13227
Read Online
ACCESS | Metrics & More | Article Recommendations | Supporting Information

ABSTRACT: The control of oxygen vacancy (V_O) formation is critical to advancing multiple metal-oxide-perovskite-based technologies. We report the construction of a compact linear model for the neutral V_O formation energy in ABO_3 perovskites that reproduces, with reasonable fidelity, Hubbard-*U*-corrected density functional theory calculations based on the state-of-the-art, strongly constrained and appropriately normed exchange-correlation functional. We obtain a mean absolute error of 0.45 eV for perovskites stable at 298 K, an accuracy that holds across a large, electronically diverse set of ABO_3 perovskites. Our model considers perovskites containing alkaline-earth metals (Ca, Sr, and Ba) and lanthanides (La and Ce) on the A-site and 3*d* transition metals (Ti, V, Cr, Mn, Fe, Co, and Ni) on the B-site in six different crystal systems (cubic, tetragonal, orthorhombic, hexagonal, rhombohedral, and monoclinic) common to perovskites. Physically intuitive metrics easily extracted from existing experimental thermochemical data or via inexpensive quantum mechanical calculations, including crystal bond dissociation energies and (solid phase) reduction potentials, are key components of the model. Beyond validation of the model against known experimental trends in materials used in solid oxide fuel cells, the model yields new candidate perovskites not contained in our training data set, such as $(Bi,Y)(Fe,Co)O_3$, which we predict may have favorable thermochemical water-splitting properties. The confluence of sufficient accuracy, efficiency, and interpretability afforded by our model not only facilitates high-throughput computational screening for any application that requires the precise control of V_O concentrations but also provides a clear picture of the dominant physics governing V_O formation in metal-oxide perovskites.

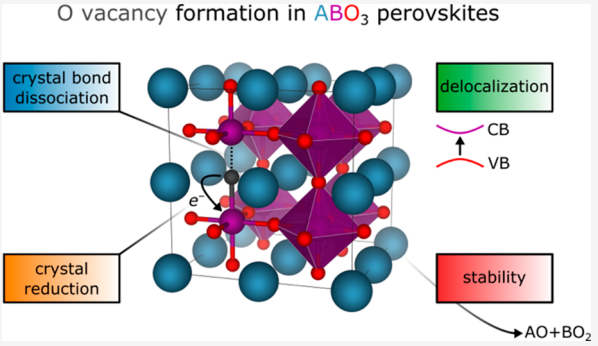

INTRODUCTION

Metal-oxide perovskites have many applications in fields ranging from energy science to electronics: e.g., two-step thermochemical cycles for water and carbon dioxide splitting (WS and CDS, respectively),[1−7] thermochemical energy storage,[8−11] thermochemical O_2 storage/pumping,[12−14] thermochemical air separation,[14−18] clean electricity production using solid oxide fuel cells (SOFCs),[19−23] solid oxide electrolyzers that produce hydrogen and carbon monoxide from high-temperature electrochemical WS and CDS,[24−26] and ferroelectric random-access memory (FRAM).[27−29] These applications depend sensitively on the concentration of oxygen vacancies (V_Os), which are capable of dictating thermodynamic, electronic, and emergent properties. As examples, V_Os reduce H_2O to H_2 in a two-step thermochemical WS (often referred to as solar thermochemical hydrogen or STCH),[2,30,31] absorb O_2 to maintain low O_2 partial pressures in thermochemical O_2 storage/pumping and air separation,[12−14] facilitate O^{2-} transport in SOFCs,[22,23,32,33] and pin ferroelectric domain walls that impede ferroelectric switching in FRAM.[34−37] The concentration of V_Os in any given oxide chiefly depends on their formation energy (E_v), which is a well-vetted microscopic descriptor of performance, especially in applications such as STCH[38−40] and SOFCs.[22,23,33,41]

The ease with which a neutral V_O forms in metal (M) oxides, where a neutral V_O refers to the removal of an entire oxygen atom (in its neutral, ground-state $^3P_2$ electron configuration) that contributes to half of an O_2 gas molecule (in its neutral, ground-state $^3\sum_g^-$), leaving behind two electrons from the O^{2-} that are donated back to the lattice (typically the cation sublattice), can be described by the following simple physical picture, similar to an extended Born−Haber cycle (see Figure 1).[22,23] First, forming the V_O breaks bonds (*O−M bond dissociation*). Second, the neutral V_O may reduce its neighboring cations (*M reduction*) or, in materials with aliovalent substitution (e.g., Sr-substituted $LaMO_3$), may fill partial holes in the O *sp* band (*lattice reduction*).[42−47] Third, intrinsic stability/instability can predispose the metal oxide to form fewer/more V_Os (*metal oxide stability*).[48−50] Note that stability typically is assessed as the energy above the convex hull (E_{hull}), which is the energy of

Received: May 30, 2021
Published: August 16, 2021

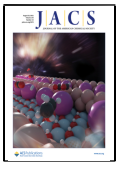

https://doi.org/10.1021/jacs.1c05570
J. Am. Chem. Soc. 2021, 143, 13212−13227

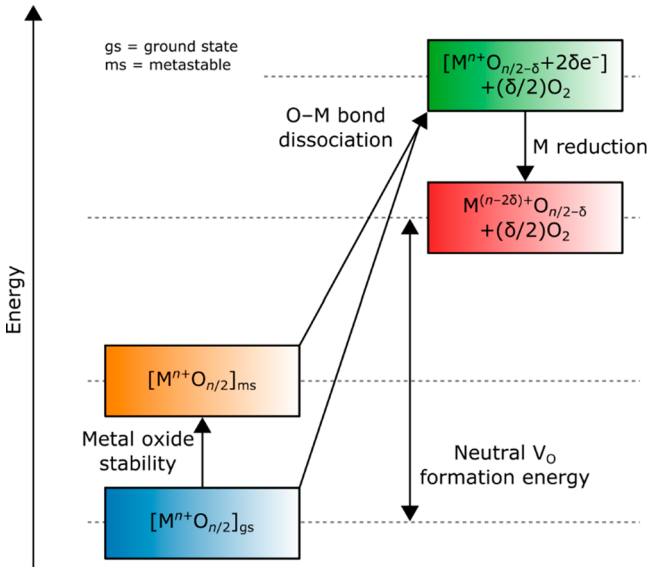

Figure 1. Picturing neutral V_O formation in metal (M) oxides as an extended Born–Haber thermodynamic cycle. With the metal oxide in its ground-state (gs) polymorph as the starting point, neutral V_O formation involves O–M bond dissociation typically followed by M reduction. Metastability (ms) of the underlying metal oxide can lead to a decrease in the neutral V_O formation energy.

decomposition of a given material into the set of most stable materials at its chemical composition.

To better understand the nuances of and optimize V_O formation in metal oxides, we need deeper understanding of crystal and electronic structure–property relationships. To this end, many have turned to density functional theory (DFT) based calculations coupled with phenomenological model building.[33,51−69] The literature contains a number of models capable of predicting V_O formation energies: e.g., those based on the O 2*p* band center descriptor.[33,51,62−66] It is important, however, to contrast the strengths of these models with their limitations, in order to illustrate our motivation for building an improved model in terms of physical intuition and ease of calculation.

In terms of strengths, these models generally are quite accurate. For example, Lee et al. introduced the O 2*p* band center as a descriptor for the V_O formation energy and applied it to the discovery of new multinary perovskites for SOFCs that were verified experimentally.[33] Deml et al. reported a mean absolute error (MAE) of ∼0.2 eV for 45 insulating binary and ternary metal oxides using computable quantities such as formation enthalpies, electronic band centers, and Pauling electronegativities.[66] Pavone et al.[23] showed, and Maiti et al.[52] later confirmed, that atomic properties, such as ionization energies and bond dissociation enthalpies, can be used to make predictions in perovskite crystals with surprising accuracy, given the dissimilarity between the chemical environments of atoms/molecules and solid crystals. Most of these models are simple, i.e., they contain only a few terms or descriptors, which suggests that V_O formation energies are readily describable. While some of the prior model predictions have been validated experimentally, leading to the discovery of new materials for a variety of applications,[33,52] significant progress is still required in the case of applications such as STCH (driven directly by solar or potentially other sources of renewable heat) to achieve improved efficiencies.

Despite their strengths, the reported models are still limited in a number of ways. The first limitation has to do with the level(s) of DFT used for parametrization. A few models[52,59] have been constructed using the generalized gradient approximation (GGA) exchange-correlation (XC) functional of Perdew, Burke, and Ernzerhof (PBE).[70] While PBE XC can describe alkaline-earth and La oxides fairly accurately (*vide infra*), this method fails for 3*d*-transition-metal oxides, where a more accurate treatment of XC is essential.[71] The most widely used method is PBE+*U*, which pairs the PBE XC functional with Hubbard *U* corrections to reduce the large self-interaction error incurred by highly localized *d* electrons in transition-metal cations.[71] However, the state-of-the-art XC functional for solids is the strongly constrained and appropriately normed (SCAN) meta-GGA XC functional.[72,73] We recently showed that an accurate reproduction of the properties of transition-metal oxides using the SCAN functional still requires Hubbard *U* corrections:[74−76] i.e., a SCAN+*U* approach. Our methodology, in which we fit *U* to relevant oxidation energies,[77,78] provides superior predictions of bulk thermodynamics, band gaps, and magnetic structures in comparison to PBE, PBE+*U*, and SCAN, thus highlighting the usefulness of a database of SCAN+*U* V_O formation energies that we present herein.

The second major limitation of the existing models is that they, to the best of our knowledge, were trained on homogeneous subsets of perovskite chemical space. Specifically, they lack a diverse sampling of A- and/or B-site metal cations (# unique A × # unique B ≤ 10),[33,57,59−61,64,65] space groups (# unique = 1),[33,51,52,59,60,63−65] and electronic structures (i.e., metals, semimetals, and nonmetals).[66,69] The only exception is the study by Maiti et al.,[52] which uses the less accurate PBE XC functional for 3*d*-transition-metal-containing perovskite oxides. The lack of diversity in the training data can significantly limit the predictive power of such models, especially when they are extrapolated to higher-component (e.g., quaternary, quinary, etc.[7]) and structurally diverse (e.g., experimentally accessible metastable polymorphs[79−81]) metal-oxide chemical spaces.

Finally, model-building approaches that use the band center or band gap as descriptors often rely on computationally expensive hybrid functional or GW calculations to obtain accurate predictions, which makes it hard to train a large data set. Moreover, band-center-based descriptors lack the physical intuition with respect to the physical process of V_O formation (i.e., M–O bond dissociation, reduction, and stability), as the band *edges* normally play a more significant role than the band *center*. Thus, the need still exists to build a computationally inexpensive yet sufficiently accurate, more physically intuitive, and broadly trained predictive model, especially for the discovery of higher-component or structurally diverse materials.

In this work, we utilize the state-of-the-art SCAN+*U* method to construct a large database of V_O formation energies in ABO_3 perovskite oxides for a diverse collection of metal cations, i.e., A-sites (Ca, Sr, Ba, La, and Ce) and B-sites (Ti, V, Cr, Mn, Fe, Co, and Ni), and space groups (cubic, tetragonal, orthorhombic, hexagonal, rhombohedral, and monoclinic), as well as a range of electronic structures, from wide-band-gap insulators and semiconductors to metallic systems. As such, we have set out to provide an accurate (i.e., using SCAN+*U*), extensive (341 unique V_Os), and diverse (233 composition–structure combinations) catalog of V_O formation energies. Subsequently, we fit a theoretical model, using machine-learning techniques

https://doi.org/10.1021/jacs.1c05570
J. Am. Chem. Soc. 2021, 143, 13212−13227

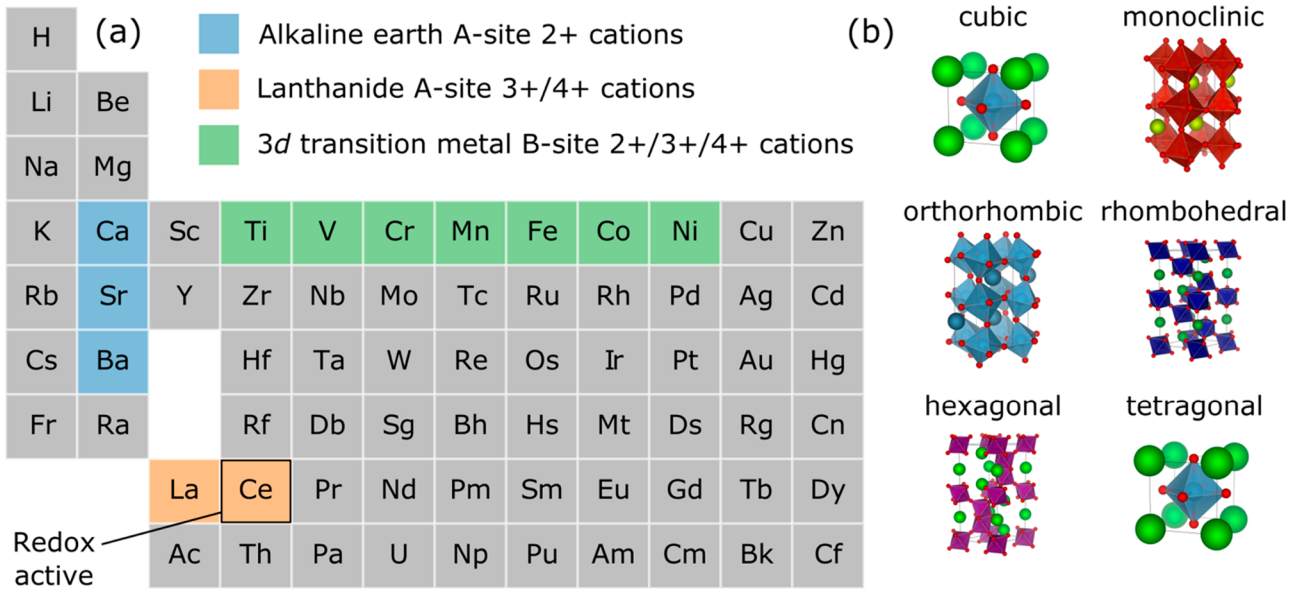

Figure 2. ABO_3 perovskite structures. Elements (panel a, non-gray rectangles) and crystal systems (panel b) considered in this study. A-sites (blue and orange) and B-sites (green) are as follows: Ca (2+), Sr (2+), Ba (2+), La (3+), Ce (3+ or 4+), Ti (3+ or 4+), V (3+ or 4+), Cr (3+ or 4+), Mn (3+ or 4+), Fe (3+ or 4+), Co (2+, 3+, or 4+), and Ni (2+, 3+, or 4+).

with simple and physically intuitive descriptors, such as crystal bond dissociation energies and crystal (i.e., solid phase) reduction potentials, to understand and predict V_O formation energies in a diverse set of metal-oxide perovskite frameworks.

The structure of this paper is as follows. First, we detail the computational methods used. Second, we explain the construction of our model and report its performance, key metrics, and trends for various subsets of the data. Third, we introduce our descriptors for V_O formation energies and explain how they improve upon the palette of descriptors used in the literature. Fourth, we outline avenues for future research, both in terms of improving our methodology and for applying it to more complex systems (e.g., multinary metal-oxide perovskites and nonoxides). We also discuss the implications of our model with a focus on materials design and candidate identification for various applications. Finally, we conclude by recapitulating our findings and their implications for the understanding and control of V_O formation in metal-oxide perovskites.

COMPUTATIONAL METHODS

Quantum Mechanics Calculations. We performed DFT+U[74−76] calculations of neutral V_O formation energies, crystal reduction potentials, phase diagrams, and band gaps using the Vienna Ab initio Simulation Package (VASP version 5.4.4).[82,83] We used the SCAN XC density functional,[72] with optimal U values taken from previous work.[77,78] To apply the Hubbard U correction, we employed the rotationally invariant scheme of Dudarev et al.[84] as implemented in VASP. We find that SCAN+U calculations are only modestly more computationally expensive (∼1.85−2.35×) for each self-consistent-field loop in comparison to those with PBE+U (see Table S1 in the Supporting Information). We utilized the all-electron, frozen-core, projector augmented-wave (PAW) potentials[85,86] as in our prior work[7,77,78,87] to describe the ion-electron interactions, along with including the nonspherical contributions related to the gradient of the electron density and the kinetic energy density within the PAW spheres for the XC evaluation. We used the *Accurate* "precision" mode in VASP to avoid aliasing errors when the fast-Fourier-transform and support grids were set, employed an additional support grid for more accurate evaluation of augmentation charges, and evaluated the projection operators in real space using VASP's fully automatic optimization scheme. We used a plane-wave kinetic energy cutoff of 520 eV,[7,77,78,87] as this threshold converges total energies of oxide perovskites to within 1 meV/atom.

To perform Brillouin-zone integrations, we used a Γ-point-centered Monkhorst−Pack[88] k-mesh with spacing between k-points of ≤0.025 Å^{-1}, as previously optimized,[77] and added a Gaussian smearing function with a width of 0.05 eV. For electronic minimizations, we used the blocked Davidson iteration scheme or the conjugate gradient algorithm,[89] depending on difficulties in convergence. In all cases, we deemed to have reached self-consistent-field convergence when the energy change between steps was ≤1×10^{-5} eV/cell. We performed collinear, spin-polarized calculations and initialized the atomic magnetic moments in a ferromagnetic configuration.[39,90] We considered the high-spin states for Ti, V, Cr, Mn, Fe, Co, and Ni, while for Co and Ni, we also considered the intermediate- and low-spin states. We used the conjugate gradient algorithm to perform structure optimization, stopping the process when the norms of all the atomic forces reached ≤|0.03| eV/Å. For primitive cells, we optimized the atomic positions, cell shape, and cell volume, whereas for supercells, we only optimized the atomic positions to simulate the formation of V_Os in the dilute limit, in which the bulk lattice structure is not expected to change. Although we preserved symmetry in primitive cell structure optimizations to ensure that there were no symmetry-breaking relaxations (e.g., cubic → tetragonal), we did not preserve the symmetry of ionic positions in supercell calculations, in order to allow for local symmetry breaking upon V_O formation.

ABO_3 Perovskite Structures. Figure 2 displays the set of elements (Figure 2a) and structures (Figure 2b) that we considered in constructing our V_O formation energy data set. On the A-site, we considered alkaline-earth metals (Ca, Sr, and Ba) and lanthanides (La and Ce) that are reasonably abundant and are most likely to adopt the perovskite crystal structure (as opposed to ilmenite-like phases).[91] Of the lanthanides, we focused on La and Ce because they comprise the $La_{1-x}SrMO_3$ (M = Cr, Mn, Fe, Co) family of perovskite-type materials for SOFC applications and CeO_2, the state-of-the-art metal oxide for STCH, respectively. On the B-site, we considered the redox-active 3d transition metals (i.e., Ti, V, Cr, Mn, Fe, Co, and Ni), with the exception of Cu, since Cu oxides typically will not survive nominal STCH temperatures. SCAN/SCAN+U also inaccurately describes Cu redox chemistry.[78,92] We did not consider the 4d and 5d transition metals for two reasons, both of which we hope to address in future

https://doi.org/10.1021/jacs.1c05570
J. Am. Chem. Soc. 2021, 143, 13212−13227

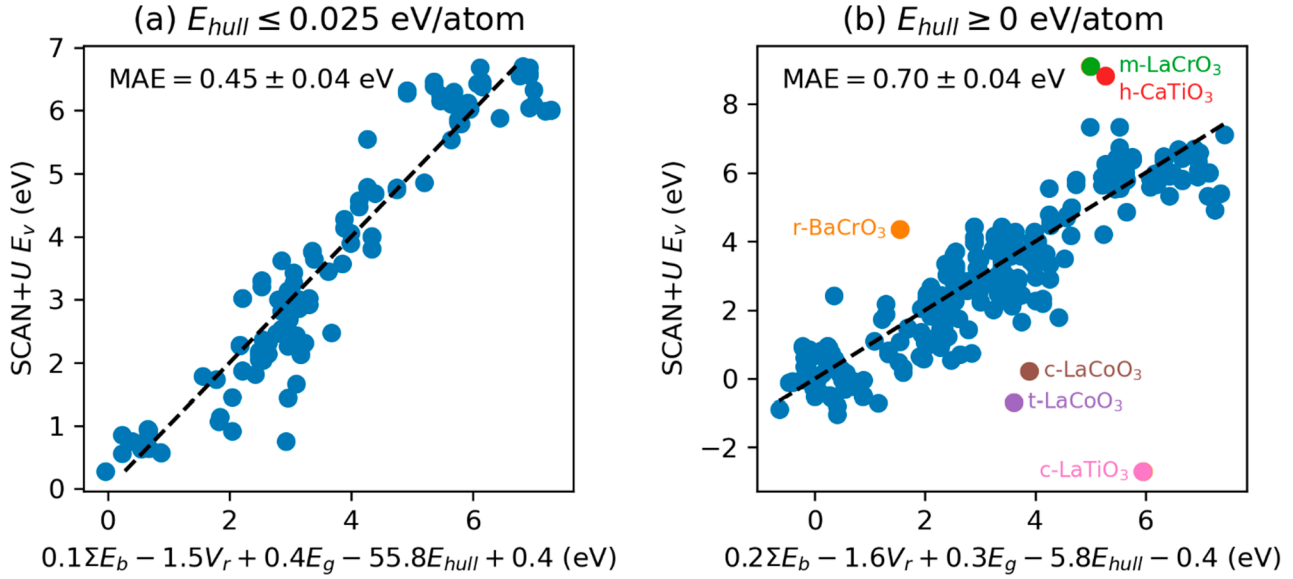

Figure 3. SCAN+*U*-calculated vs model-predicted E_v for (a) room-temperature-stable ($E_{hull} \leq 298.15k_B$) and (b) all ABO_3 perovskite structures considered. $\sum E_b$ is the crystal bond dissociation energy sum in eV, V_r is the maximum crystal reduction potential in V vs O_2 (i.e., per 1/4 mol of O_2 gas), E_g is the SCAN+*U* band gap at the Γ-point in eV, and E_{hull} is the energy above the convex hull in eV/atom. Non-blue markers correspond to qualitative outliers. The dashed black line corresponds to perfect agreement between SCAN+*U* and the model.

work: (1) we have not yet evaluated optimal *U* values for their oxides within the SCAN+*U* framework and (2) we wanted to make the construction of our database computationally tractable. For each composition, we considered the following six lattice systems (in Hermann−Mauguin[93] notation) common to perovskites in the Inorganic Crystal Structure Database (ICSD):[94] cubic (e.g., *Pm*$\bar{3}$*m* $SrTiO_3$, ICSD #181652), hexagonal (e.g., $P6_3/mmc$ $SrMnO_3$, ICSD #185417), rhombohedral (e.g., *R*3*c* $LaCrO_3$, ICSD #167590), tetragonal (e.g., *P*4*mm* $BaTiO_3$, ICSD #164388), orthorhombic (e.g., *Pnma* $CaTiO_3$, ICSD #165801), and monoclinic (e.g., $P2_1/b$ $CeVO_3$, ICSD #162747). We used the scheme in ref 7 to obtain structures for primitive cells. Figure S1 in the Supporting Information has additional details on the composition of the data set.

***Ab Initio* Thermodynamics.** In this work, we calculated neutral V_O formation energies (E_v) in the dilute vacancy limit (see Figure S2 for the distribution of E_v and the data files for tabulated E_v values). We used the structure_matcher[95] module in pymatgen[96] to obtain all possible symmetry-distinct neutral V_O configurations. The formation energy of a neutral V_O is given by:

$$E_v = E^{SCAN+U}_{defective} - E^{SCAN+U}_{pristine} + \frac{1}{2}E^{SCAN}_{O_2} \quad (1)$$

where E^{SCAN+U} is the SCAN+*U* total energy, *pristine* is a supercell of the primitive cell, and *defective* is the same supercell with a neutral V_O. $E^{SCAN}_{O_2}$ is the SCAN total energy of an O_2 gas molecule in its ground-state triplet electronic configuration. E_v is converged to within ±0.1 eV for a 3 × 3 × 3 supercell of the cubic and tetragonal phases, 2 × 2 × 2 supercell of the orthorhombic and monoclinic phases, and 2 × 2 × 1 supercell of the hexagonal and rhombohedral phases (see Figure S3 in the Supporting Information for the convergence of E_v in different crystal systems with respect to supercell size).

For all perovskites considered, we quantified the stability with E_{hull} and tested the stability against all elemental phases (i.e., A, B, and O; XC = SCAN) and ordered (i.e., all sites in a given structure have integer atomic occupations), experimentally characterized binary and ternary metal oxides (e.g., AO, B_2O_3, AB_2O_4, etc.; XC = SCAN+*U*) containing the elements of the perovskite. For the DFT calculations of elemental solids, we used the SCAN XC functional without Hubbard *U* corrections, as the latter fails in predicting the properties of metallic systems with delocalized electrons. While DFT-SCAN and SCAN+*U* total energies are incompatible theoretically, this only influences A-rich and B-rich regions of the phase diagram that are isolated from the stability regions of the perovskite compositions we considered and only exist for the sake of completing the individual ternary phase diagrams. Therefore, the E_{hull} values reported here were calculated using a consistent theoretical treatment of all potential structures using SCAN+*U*. We used the phase_diagram module[97,98] in pymatgen[96] to generate the 0 K phase diagrams and calculate E_{hull} (see Figure S4 in the Supporting Information for the distribution of E_{hull}).

To calculate crystal bond dissociation energies (*vide infra*), we first calculated cohesive energies from atomic total energies (see Figure S5 in the Supporting Information for the periodic trends in experimental cohesive energies). We tested convergence with respect to cell size (12, 16, and 20 Å) and used nearly cubic cells with minimal orthorhombic distortions to lift spurious intrashell degeneracies of atoms with partially filled shells (see Figure S6 in the Supporting Information for the cell-size convergence of atomic total energies). Our predicted magnetic moments agree with the experimental ground-state atomic electron configurations with the exception of V, which prefers $[Ar]4s^03d^5$ over $[Ar]4s^23d^3$ by 0.29 eV—this could be explained by inaccuracies of conventional spin-neutral PAW potentials.[99−103] With that being said, this only leads to a small change of 0.05 eV in the V−O crystal bond dissociation energies. Finally, we used the Huber regressor in scikit-learn[104] for supervised learning of E_v. The Huber regressor is a regularized linear regression model that is robust to outliers. While nonlinear regression may find better descriptors for many properties (e.g., symbolic regression identified a simple descriptor for the oxygen evolution reaction activity of metal-oxide perovskites[105]), we find that E_v can be described by a physically intuitive extended Born−Haber cycle (*vide infra*), justifying the use of a linear model. The coefficients, intercepts, and scores reported here were cross-validated by averaging over 1000 models trained on random permutations of 50% of the data.

RESULTS

Model for V_O Formation in Metal-Oxide Perovskites. First, we report the performance of and key metrics in our best E_v model for room-temperature-stable ($E_{hull} \leq 0.025$ eV/atom $\approx 298.15\text{K}\cdot k_B$, where k_B is the Boltzmann constant) perovskites, as well as all perovskites considered. Figure 3 shows the agreement between SCAN+*U*-calculated (vertical axis) and model-predicted (horizontal axis) E_v values for 142 unique V_Os

https://doi.org/10.1021/jacs.1c05570
J. Am. Chem. Soc. 2021, 143, 13212−13227

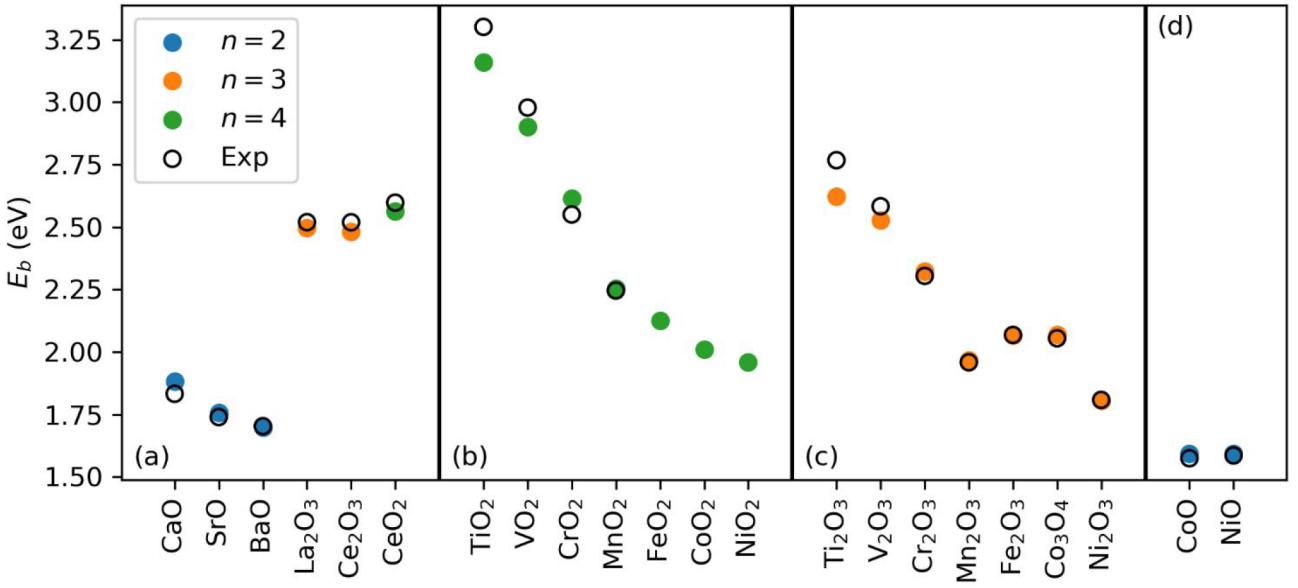

Figure 4. Specific trends in the SCAN+U-calculated and experimental E_b values vs (a) A-site atoms (+2/+3/+4) oxidation states, (b) B-site atoms (+4), (c) B-site atoms (+3), and (d) B-site atoms (+2). Experimental formation energies/enthalpies are not available for metastable FeO_2, CoO_2, and NiO_2.

in room-temperature-stable perovskites (Figure 3a) and an all-encompassing superset of 341 perovskites (Figure 3b), with SCAN+U-calculated and model-predicted values ranging from −2.69 to 9.11 eV and from −0.65 to 7.44 eV, respectively. To the best of our knowledge, this constitutes the most comprehensively trained model for perovskite E_v values to date. The model is linear with four intuitive energy terms, which we describe in more depth below: crystal bond dissociation energy sum ($\sum E_b$), maximum crystal reduction potential (V_r), SCAN+U band gap at the Γ-point (E_g), and the energy above the convex hull (E_{hull}). Note that the crystal system correlates indirectly with E_v via E_g and E_{hull} (see Figure S7 in the Supporting Information). The model's predictions are in good agreement with SCAN+U calculations, with MAEs of 0.45 ± 0.04 and 0.71 ± 0.05 eV for room-temperature-stable structures and all structures, respectively. Figure 3b shows that there are approximately six major qualitative outliers (nonblue markers), which we will address in the Discussion.

Crystal Feature Engineering Used in the Model. *Crystal Bond Dissociation Energy.* The inspiration for $\sum E_b$ stems from its molecular analogue, bond dissociation energies (BDEs), for which experimental values are widely available in references such as the *CRC Handbook of Chemistry and Physics*.[106] For transition-metal (M) oxides, however, experimental BDEs are only available for diatomic molecules/cations, e.g., MO(g) and MO^+(g), which lack the inclusion of effects from the metal's oxidation state and the crystal field of the solid. To incorporate these effects, we define a crystal O^{2-}−M^{n+} bond dissociation energy (E_b) as:

$$E_b[O^{2-}\text{–}M^{n+}] = E_c[MO_{n/2}]/N_b[O^{2-}\text{–}M^{n+}] \quad (2)$$

where n is the oxidation state of M, $E_c[MO_{n/2}]$ is the cohesive energy of the ground-state polymorph of the binary oxide crystal containing M^{n+}, and $N_b[O^{2-}\text{–}M^{n+}]$ is the number of O^{2-}−M^{n+} bonds per $MO_{n/2}$ formula unit. E_b can be thought of as the cohesive energy per bond in an ionic oxide framework or the energy required to fully break an O^{2-}−M^{n+} bond. We use the E_c values of ground-state binary-oxide polymorphs because they provide a consistent (upper) limit on E_b and they can be extracted from either experiment or theory.

To calculate E_b, consider the following series of chemical reactions:

$$MO_{n/2}(s) \rightarrow M(s) + (n/4)O_2(g), \quad -\Delta E_f[MO_{n/2}] \quad (3a)$$

$$M(s) \rightarrow M(g), \quad E_c[M] \quad (3b)$$

$$(n/4)O_2(g) \rightarrow (n/2)O(g), \quad (n/4)BDE[O_2] \quad (3c)$$

$$MO_{n/2}(s) \rightarrow M(g) + (n/2)O(g)$$

$$E_c[MO_{n/2}] = -\Delta E_f[MO_{n/2}] + E_c[M] + (n/4)BDE[O_2] \quad (3d)$$

where $\Delta E_f[MO_{n/2}]$ is the binary metal-oxide formation energy/enthalpy, $E_c[M]$ is the cohesive energy of the pure metal element, and $BDE[O_2]$ is the bond dissociation energy of O_2 per atom. The energy change for the net reaction (eq 3d) is $E_c[MO_{n/2}]$. The experimental $E_c[MO_{n/2}]$ value can be calculated from the experimental $\Delta E_f[MO_{n/2}]$,[107−111] $E_c[M]$,[112] and $BDE[O_2]$ values.[106] The experimental $N_b[O^{2-}\text{–}M^{n+}]$ value can be obtained from the experimental binary-oxide crystal structures, which can be found in crystallographic databases such as the ICSD.[94] In the absence of experimental data, theoretical $E_c[MO_{n/2}]$ and $N_b[O^{2-}\text{–}M^{n+}]$ values can be computed from SCAN+U total energies and optimized crystal structures, which are available in computational databases such as the Materials Project (MP),[113] Open Quantum Materials Database (OQMD),[114,115] and Automatic−FLOW for Materials Discovery (AFLOW).[116] Note that because we define E_b for stable binary metal oxides, namely their ground-state polymorphs, ternary instabilities are captured primarily by E_{hull}.

As an example, take the $E_b[O^{2-}\text{–}Ce^{4+}]$ value for CeO_2, where we are given that M = Ce, n = 4, $MO_{n/2} = CeO_2$, and its ground-state polymorph adopts the fluorite structure ($Fm\bar{3}m$). According to the net reaction in eq 3d, the theoretical E_c value is given by:

https://doi.org/10.1021/jacs.1c05570
J. Am. Chem. Soc. 2021, 143, 13212−13227

$$E_c[CeO_2] = E^{SCAN+U}[Ce] + 2E^{SCAN}[O] - E^{SCAN+U}[CeO_2] \quad (4)$$

where $E^{SCAN+U}[Ce]$ and $E^{SCAN}[O]$ are the SCAN+U and DFT-SCAN total energies of gaseous neutral Ce and O in their ground-state $^1G_4$ and $^3P_2$ electron configurations, respectively,[117] and $E^{SCAN+U}[CeO_2]$ is that of fluorite CeO_2. Note that using SCAN+U instead of DFT-SCAN to calculate the total energy of an isolated, neutral Ce atom is appropriate, since Ce is metallic only in its bulk solid ground state and the tightly held open-shell d and f electrons require the Hubbard U correction to mitigate the self-interaction error within DFT. That said, the $^1G_4$ atomic state is an open-shell singlet state (coupling a 4f and a 5d electron), requiring two determinants to properly describe its spin coupling. Instead, single-determinant DFT+U theory only describes a spin-polarized, spin-contaminated singlet. As it turns out, the E_c error caused by this spin contamination is acceptably small: the theoretical and experimental $E_c[CeO_2]$ values are in good agreement (20.51 and 20.78 eV/formula unit, respectively), with an absolute error (AE) of 0.09 eV/atom across all metal oxides considered (see Table S2 in the Supporting Information). Here, the experimental E_c is given by the formula in eq 3d. Since O^{2-} is tetrahedrally coordinated to four Ce^{4+} atoms and there are two O^{2-} atoms per formula unit of CeO_2, N_b = 8. Inserting E_c and N_b into eq 2 yields theoretical and experimental $E_b[O^{2-}-Ce^{4+}]$ values of 2.56 and 2.60 eV/bond, respectively (AE = 0.04 eV). Interestingly, the experimental $E_b[O^{2-}-Ce^{4+}]$ value is 3.15−3.40 times smaller than its molecular analogues, BDE[CeO(g)] (8.19 eV at 298 K) and BDE[CeO^+(g)] (8.83 ± 0.16 eV at 298 K).[106] Ce in CeO_2(s) donates its four valence electrons ($6s^25d^14f^1$) equally among its nearest O neighbors, within the electrostatic potential of the CeO_2 crystal, whereas Ce in CeO(g) and CeO^+(g) shares its electrons with only one O absent any other potential, creating up to a triple M−O bond in the diatomic species.[118] Additionally, differences in the ionic characters of the $O^{2-}-Ce^{4+}$, O−Ce (i.e., ≈ $O^{2-}-Ce^{2+}$), and O−Ce^+ (i.e., ≈$O^{2-}-Ce^{3+}$) bonds in CeO_2(s), CeO(g), and CeO^+(g), respectively, also contribute to the deviation between molecular and crystal BDEs.

Figure 4 shows the specific trends in the theoretical E_b values (vertical axis) for the ground-state $MO_{n/2}$ (horizontal axis) of the A- and B-site cations that we considered. The experimental (unfilled markers) and theoretical (filled markers) E_b values are in good agreement, with MAE = 0.04 eV, indicating that the former can be used when the latter are unavailable (or vice versa), without loss of accuracy. For the A-site cations (Figure 4a), the theoretical E_b trend from strong to weak crystal bonds is Ce^{4+} (2.56 eV) > La^{3+} (2.50 eV) > Ce^{3+} (2.48 eV) > Ca^{2+} (1.88 eV) > Sr^{2+} (1.76 eV) > Ba^{2+} (1.70 eV). The higher E_b values for Ce and La in comparison to those for the alkaline earths can be attributed to either (1) the higher oxidation states of Ce (+4 or +3) and La (+3), which can increase the magnitude of the electrostatic potential energy associated with each bond, or (2) the greater number of electrons per bond for CeO_2 (0.5 e^-/bond) in comparison to La_2O_3/Ce_2O_3 (0.43 e^-/bond) and CaO/SrO/BaO (0.33 e^-/bond). Additionally, the increasing size mismatch between A^{2+} and O^{2-} from Ca^{2+} to Ba^{2+} results in a weaker electrostatic attraction, leading to weaker crystal bonds, thus explaining the observed trend in E_b.

For the B^{4+} cations (Figure 4b), the theoretical E_b values display a monotonically decreasing trend as B progresses from Ti to Ni: i.e., Ti^{4+} (3.16 eV) > V^{4+} (2.90 eV) > Cr^{4+} (2.61 eV) > Mn^{4+} (2.25 eV) > Fe^{4+} (2.13 eV) > Co^{4+} (2.01 eV) > Ni^{4+} (1.96 eV). We find a similar trend for the B^{3+} cations (Figure 4c), i.e., Ti^{3+} (2.62 eV) > V^{3+} (2.53 eV) > Cr^{3+} (2.32 eV) > Fe^{3+} = $Co^{8/3+}$ (2.07 eV) > Mn^{3+} (1.97 eV) > Ni^{3+} (1.81 eV), with Fe and Co as notable exceptions. The $B^{2+}-O^{2-}$ E_b values (Figure 4d) are lower than the corresponding $B^{3+}-O^{2-}$ E_b values, which in turn are consistently lower than the respective $B^{4+}-O^{2-}$ E_b values (except for Co). Notably, Fe^{3+} is stabilized by its d^5 electron configuration, leading to a higher E_b value in comparison to Mn_2O_3. On the other hand, the E_b value for $Co^{8/3+}$, which is derived from $Co(II,III)_3O_4$ and acts as a proxy for the unstable $Co(III)_2O_3$, is higher than that for CoO_2, which can be attributed to the stability (metastability) of Co_3O_4 (CoO_2). Figure S8 in the Supporting Information has additional details on E_b and its molecular analogues.

Crystal Reduction Potential. In the same spirit as $\sum E_b$, V_r extends useful concepts from atomic/molecular (electro)chemistry, such as ionization energies (E_i) and standard reduction potentials ($V°$), to the solid state by consistently including crystal field effects and removing any solvation effects in an aqueous (or other liquid) medium. Another motivation for V_r stems from the unavailability of experimental $V°$ values for the following reduction reactions, relevant in ABO_3 perovskites: $Fe^{4+} \rightarrow Fe^{3+}$ and $Ni^{4+} \rightarrow Ni^{3+}$.[106] We define a crystal $M^{n+} \rightarrow M^{m+}$ (where $n > m$) reduction potential (V_r) vs O_2 (per 1/4 mol of O_2 gas) as:

$$V_r[M^{n+} \rightarrow M^{m+}] = -E_r[M^{n+} \rightarrow M^{m+}]/(n-m)F \quad (5)$$

where n and m are the oxidation states of the oxidized and reduced metals in the ground-state polymorphs of their binary metal-oxide crystals $MO_{n/2}$ and $MO_{m/2}$, respectively, F is the Faraday constant, and:

$$E_r[M^{n+} \rightarrow M^{m+}] = E^{SCAN+U}[MO_{m/2}] + (n-m)E^{SCAN}[O_2]/4 - E^{SCAN+U}[MO_{n/2}] \quad (6)$$

Note that V_r in eq 5 is strictly defined for the Gibbs energy of reduction, which we approximate here as the internal energy (i.e., $G \approx E$), ignoring $p-V$ and entropic effects, in order to apply our scheme readily to large data sets.

V_r can be interpreted as the reduction potential of a metal cation in a crystal. For example, consider $V_r[Ce^{4+} \rightarrow Ce^{3+}]$, where M = Ce, n = 4, m = 3, $n-m$ = 1, $MO_{n/2}$ = CeO_2 (ground-state polymorph = fluorite structure, $Fm\bar{3}m$), and $MO_{m/2}$ = $CeO_{3/2}$ = $^1/_2Ce_2O_3$ (ground-state polymorph = hexagonal lattice, $P\bar{3}m1$). Following from eq 6, the theoretical E_r value is:

$$E_r[Ce^{4+} \rightarrow Ce^{3+}] = \frac{1}{2}E^{SCAN+U}[Ce_2O_3] + E^{SCAN}[O_2]/4 - E^{SCAN+U}[CeO_2] = 1.82 \text{ eV} \quad (7)$$

On the other hand, the experimental E_r = $^1/_2\Delta E_f[Ce_2O_3]$ − $\Delta E_f[CeO_2]$ = 1.86 eV.[77] Inserting E_r, $n-m$ = 1, and F into eq 5 yields theoretical and experimental V_r values of −1.82 and −1.86 V per 1/4 mol of O_2, respectively (AE = 0.04 V per 1/4 mol of O_2). Thus, reducing Ce^{4+} to Ce^{3+} in its bulk oxide state

https://doi.org/10.1021/jacs.1c05570
J. Am. Chem. Soc. 2021, 143, 13212−13227

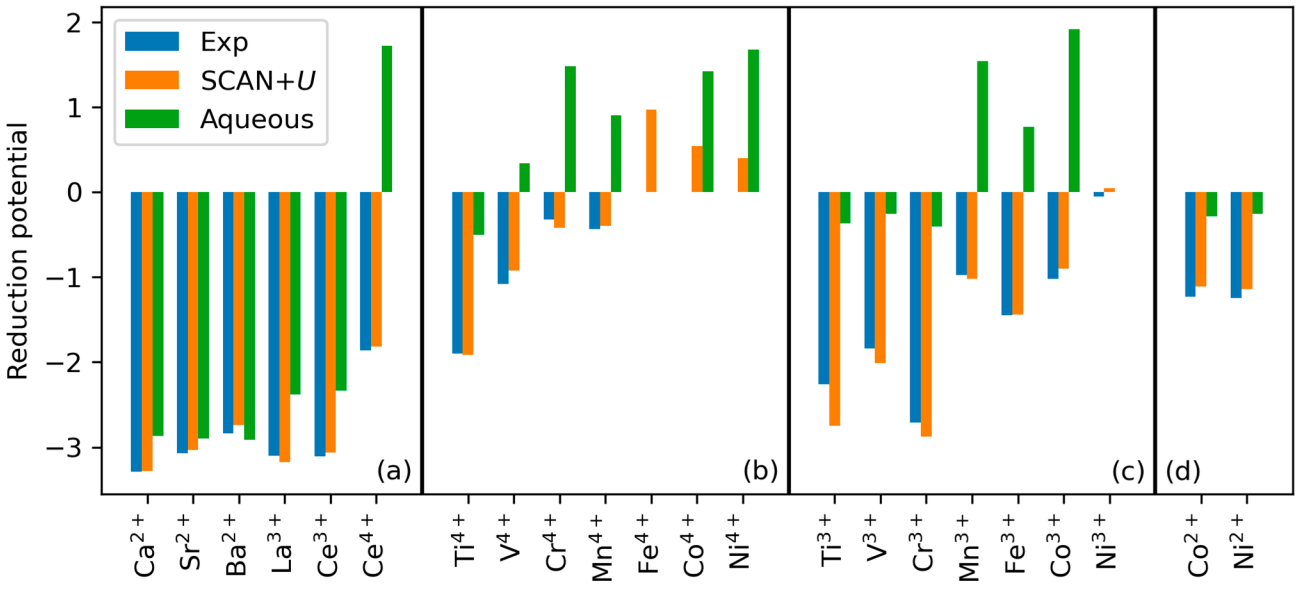

Figure 5. Comparison of experimental (blue) and theoretical (orange) V_r values with respect to available experimental aqueous standard reduction potentials (green),[106] showing that the qualitative trends are obeyed. Experimental $V°$ values are not available for $Fe^{4+/3+}$, $Ni^{4+/3+}$, and $Ni^{3+/2+}$.

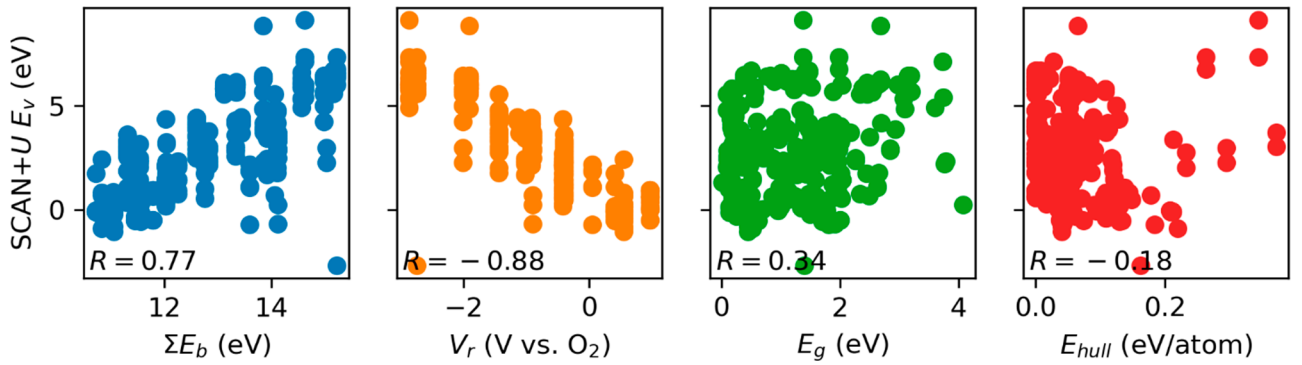

Figure 6. Relationship between SCAN+*U*-predicted E_v and $\sum E_b$ (blue), V_r (orange), E_g (green), and E_{hull} (red). The numerical ranges of the first three descriptors (i.e., the difference between the largest and smallest horizontal axis values) are approximately equal (i.e., ∼5 eV or V). V_r captures most of the contribution to E_v.

should theoretically (experimentally) require a reduction potential of 1.82 V (1.86 V) per 1/4 mol of oxygen gas.

Figure 5 shows that the experimental (blue bars) and theoretical (orange bars) V_r values are in good agreement, with MAE = 0.10 V vs O_2, implying that, like E_b, experimental values can be used to make accurate predictions in the absence of theoretical data (and vice versa). The aqueous $V°$ values (green bars), however, poorly capture the qualitative trends in V_r. Note that we plot $V°$ with respect to the standard hydrogen electrode, whereas both theoretical and experimental V_r values are plotted with respect to 1/4 mol of O_2(g). While the $V°$s of the transition-metal cations (Figure 5b−d) capture most of the trends in V_r (but have the wrong sign for V^{4+}, Cr^{4+}, Mn^{4+}, Mn^{3+}, Fe^{3+}, and Co^{3+}), those of the alkaline-earth-metal and lanthanide cations (Figure 5a) do not. Hence, it is critical to use V_r and not $V°$ values because the latter lack the consistent inclusion of crystal field effects required for a quantitatively accurate description of solid-state cation reduction. For specific trends in V_r, please see Figure S9 in the Supporting Information.

Model Intuition. Having presented E_b and V_r as descriptors for E_v and clarified how they relate to fundamental chemical concepts and principles, we now inspect the model's construction and offer intuitive rationalizations for the signs and magnitudes of its coefficients (c). Our model consists of four terms (Figure 3), $\sum E_b$ representing the energy penalty of breaking bonds and eventually creating an O_2 molecule from an O^{2-} ion (*O−M bond dissociation* in Figure 1), V_r quantifying the energy required to reduce "adjacent" cations due to the electrons left behind by the removed O^{2-} (*M reduction* in Figure 1), E_g signifying the band structure cost of placing additional electrons in an oxygen-deficient perovskite in its conduction band (not shown in Figure 1 but affects *M reduction*), and E_{hull} highlighting the impact of the underlying (in)stability of the structure in controlling V_O formation (metal oxide stability in Figure 1). Our model, with energy terms related to atomization ($\sum E_b$), ionization (V_r), and polarity of chemical bonds (E_g), can be considered to be an extended Born−Haber cycle.

The first term, $\sum E_b$, is the sum of the E_b values for the crystal bonds formed between a specific O^{2-} that forms the vacancy and its nearest cation neighbors. For perovskites:

$$\sum E_b = 4E_b[O^{2-}{-}A^{n+}] + 2E_b[O^{2-}{-}B^{m+}] \quad (8)$$

https://doi.org/10.1021/jacs.1c05570
J. Am. Chem. Soc. 2021, 143, 13212−13227

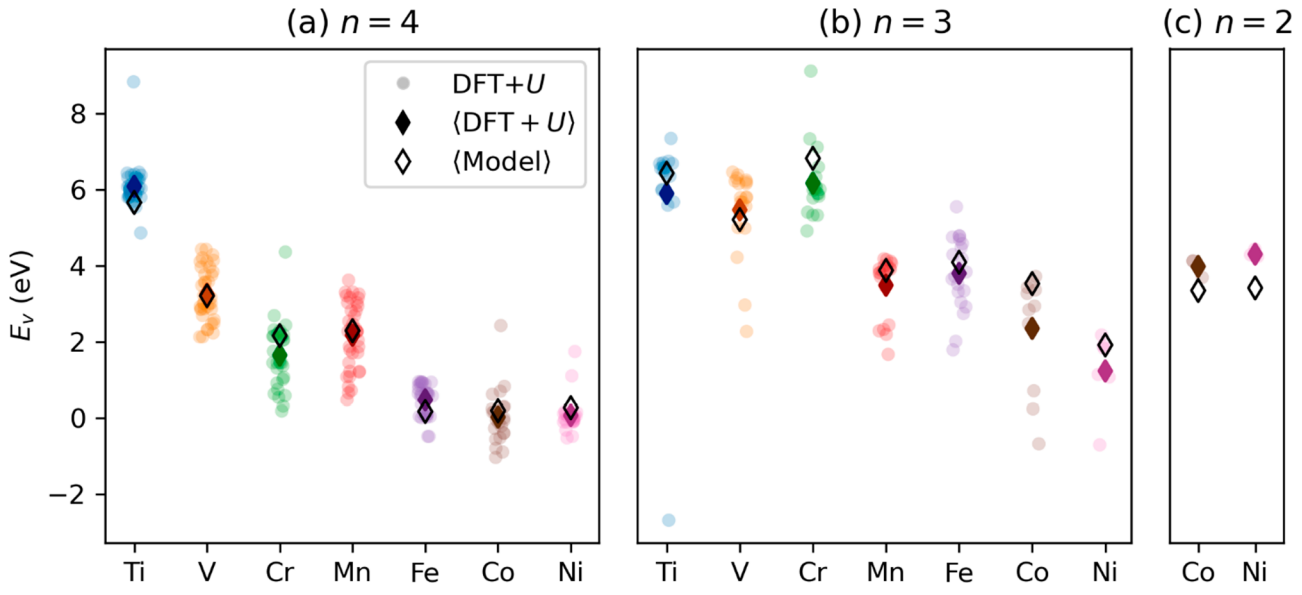

Figure 7. Specific trends in the SCAN+*U*-calculated and model-predicted E_v vs B for oxidation states (a) $n = 4$, (b) $n = 3$, and (c) $n = 2$.

because there are four O^{2-}–A^{n+} and two O^{2-}–B^{m+} crystal bonds per O^{2-}. Note that our definition of $\sum E_b$ is quite general and easily extends to any desired metal-oxide material. The sign of the E_b coefficient, $c_b > 0$, is consistent with the intuition that energy is required to break crystal bonds (R = 0.77, blue markers in Figure 6). The magnitude of c_b is smaller (0.1−0.2) than those of the other coefficients (0.3−55.8, $c_b < c_g < |c_r| < |c_{hull}|$), suggesting that $\sum E_b$ serves primarily as a correction factor to other terms in the model. Differences between the bond orders in binary and ternary oxides also can affect the magnitude of c_b; quantifying such effects will be the focus of future work.

The second term, V_r, is the maximum V_r value among the nearest cation neighbors of a specific O^{2-} and is the most dominant factor determining E_v in our model. Indeed, E_v anticorrelates quite strongly with V_r (orange markers in Figure 6), with $R = -0.88$. Choosing the maximum V_r, we assume that the most reducible nearest cation neighbor undergoes reduction and hence governs the V_r contribution to E_v. For perovskites:

$$V_r = \max(V_r[A^{m+} \rightarrow A^{n+}], V_r[B^{r+} \rightarrow B^{s+}]) \quad (9)$$

where $m > n$ and $r > s$. The sign (<0) and magnitude (1.5−1.6) of the V_r coefficient (c_r) resembles the energy for an N-electron reduction reaction, $E_r = -NV_r$, where $N = 2$, $N < 2$, and $N \ll 2$ for V_O formation in ionic, ionic + covalent, and metallic oxides, respectively. Therefore, $-c_r$ can be interpreted physically as the number of electrons donated by a specific O^{2-} to its most reducible nearest cation neighbors upon V_O formation in an ionic + covalent metal oxide.

Electrons from the departing oxygen that are left behind occupy the conduction band rather than the valence band. Hence the band gap qualitatively describes the cost of adding electrons to the conduction band upon reduction, which results in the coefficient of the third term, E_g, $c_g > 0$ (R = 0.34, green markers in Figure 6). Note that this gap is the one at the Γ-point obtained from a fully self-consistent SCAN+*U* calculation. Typical band structure and density of states calculations involve a non-self-consistent calculation after the completion of a fully self-consistent calculation. However, to minimize computational costs, we have not performed a non-self-consistent calculation, which is sufficient for our purposes here. Since the numerical ranges of the first three descriptors are approximately equal, the magnitude of c_g (0.3−0.4) signifies that E_g has a 15−20% weight to the overall E_v.

Finally, the E_{hull} coefficient, $c_{hull} < 0$ (R = −0.18, red markers in Figure 6), reflects the intuition that instability favors decomposition: e.g., via facile V_O formation. Note that the c_{hull} coefficients do vary significantly (5.5−55.8) between our models trained on room-temperature-stable and all perovskites in our data set, likely offsetting the actual E_{hull} values that are used in the room-temperature-stable ($E_{hull} \leq 25$ meV/atom) and the full (no upper limit on E_{hull}) perovskite sets. In both of our theoretical models, c_{hull} exhibits the highest magnitude of the coefficients; however, the typical values of E_{hull} for crystals are in the range of 0−100 meV/atom, which is at least one order of magnitude lower than E_b, V_r, or E_g, resulting in a significantly smaller contribution for those structures that are stable ($E_{hull} = 0$) and mildly unstable ($E_{hull} \approx 50$ meV/atom). Importantly, ours is the first modeling work to include the effects of thermodynamic (in)stability on V_O formation via E_{hull}, which could be a source of the inaccuracy and/or nonintuitiveness of previous models.[33,51−69]

B-Site Trends for Materials Design and Candidate Identification. In this section, we discuss the specific trends in the SCAN+*U*-calculated and model-predicted E_v with respect to changes in B and its oxidation state (n), focusing on materials design and candidate identification for various applications. Figure 7 shows the SCAN+*U*-calculated E_v distribution (DFT+*U*, circles), average SCAN+*U*-calculated E_v values (⟨DFT+*U*⟩, filled diamonds), and average model-predicted E_v values (⟨Model⟩, unfilled diamonds, vertical axis) as a function of B (horizontal axis) and n (panels). Overall, the average SCAN+*U*-calculated and model-predicted $\langle E_v \rangle$ values are in good agreement (MAE = 0.45 eV). For $n = 4$ (i.e., B^{4+}), $\langle E_v \rangle$ decreases in the order Ti > V > Mn ≈ Cr > Ni > Co ≈ Fe (Figure 7a), which largely coincides with increasing $V_r[B^{4+} \rightarrow B^{3+}]$ (R = −0.98): namely, Ti (−1.91 V vs O_2) < V (−0.92 V vs O_2) < Cr (−0.42 V vs O_2) ≈ Mn (−0.40 V vs O_2) < Ni (0.40 V vs O_2) < Co (0.55 V vs O_2) < Fe (0.97 V vs O_2).

https://doi.org/10.1021/jacs.1c05570
J. Am. Chem. Soc. 2021, 143, 13212−13227

Table 1. List of Promising Perovskites for STCH[a]

A	B	$\sum E_b$	V_r	E_g	space group	model E_v (eV)	T_m (K)
Y^{3+}	Fe^{3+}	16.23	−1.45	2.43[131] (exptl)	*Pnma*	4.76	1993[132]
Y^{3+}	Co^{3+}	16.23	−1.02	1.48[133] (theor)	*Pnma*	4.34	n/a
Bi^{3+}	**Fe^{3+}**	**10.71**	**-0.99**	**2.50[134] (exptl)**	***R3c***	**3.99**	**1234−1336[135]**
Bi^{3+}	**Co^{3+}**	**10.71**	**-0.99**	**1.70[136] (exptl)**	***P4mm***	**3.80**	**729[126]**

[a]Compounds in boldface type might exhibit simultaneous reduction of the A- and B-site cations. The model E_v value is calculated from the experimental $\sum E_b$ value (using eq 8), experimental V_r value (using eq 9), experimental (exptl) or theoretical (theor) E_g value, and MP PBE+*U*-calculated E_{hull} value (not listed because all $E_{hull} \approx 0$). We include the measured melting temperatures (T_m) of the candidates because thermal stability is also a significant screening criterion for STCH.

Similarly, for $n = 3$ (i.e., B^{3+}), the $\langle E_v \rangle$ trend (Figure 7b) nearly exactly anticorrelates with that of $V_r[B^{3+} \rightarrow B^{2+}]$ ($R = -1.00$): Cr (−2.87 V vs O_2) < Ti (−2.75 V vs O_2) < V (−2.01 V vs O_2) < Fe (−1.44 V vs O_2) < Mn (−1.02 V vs O_2) < Co (−0.90 V vs O_2) < Ni (0.05 V vs O_2). Finally, for Co and Ni, Figure 7a−c shows that E_v increases with decreasing n, which is consistent with the relative instability of their higher oxidation states.

For simplicity in the discussion of materials design strategies, we bin E_v into three discrete ranges: low E_v ($E_v \leq 2.5$ eV), intermediate E_v ($2.5 < E_v \leq 5$ eV), and high E_v ($E_v > 5$ eV). Low-E_v oxides are more ideal for SOFCs, thermochemical O_2 storage and pumping/separation, thermochemical energy storage, and thermochemical air separation, with optimal B-site cations being Fe^{4+}, Co^{4+}, and Ni^{4+}. While perovskites containing these cations are consistent with state-of-the-art $(La,Sr)(Co,Fe)O_3$ SOFC cathodes,[60] this reprediction of their optimality highlights the model's accuracy and potential transferability to superternary perovskite metal oxides.

Intermediate-E_v metal oxides are more suitable for STCH (WS and/or CDS) because the interactions between O^{2-} and its nearest cation neighbors should be neither too strong for extensive thermal reduction nor too weak for spontaneous water splitting. The best B-site cations for STCH are V^{4+}, Mn^{3+}, Fe^{3+}, Co^{3+}, Co^{2+}, and Ni^{2+}. Mn^{3+} appears in Ca-, Ce-, and Mn-based ABO_3 perovskites, which we recently identified to be promising candidates that potentially exhibit simultaneous reduction of both Ce^{4+} (A-site) and Mn^{3+} (B-site).[7] While the model-predicted E_v value for Mn^{4+} seems like it is too low for STCH, $BaCe_{1/4}Mn_{3/4}O_3$ is one of the best water splitters to date.[119] This underestimation is likely due to differences between its E_g value and that of $BaMnO_3$ (since Mn^{4+} is the redox-active cation in both stable materials and therefore their $\sum E_b$, V_r, and E_{hull} values should be similar), thus making band gap prediction for superternary perovskite metal oxides, an important avenue for improving the model. On the basis of these B-site cations, there are three ternary prototypes worth exploring further: (1) $A^{2+}V^{4+}O_3$, (2) $A^{3+}(Mn,Fe,Co)^{3+}O_3$, and (3) $A^{4+}(Co,Ni)O_3$. For prototype 1, while the phase impurity of oxides containing V[120−122] reduces the likelihood of its practical use, $P2_1/c$ $SrVO_3$ is a reasonable candidate with a SCAN+*U*-predicted E_v value of 3.75−3.78 eV.

For prototype 2 or 3, we used the following scheme for enumerating promising candidates, outside of our training data. First, we screened for elements known to exist most commonly in the 3+/4+ oxidation state.[123] Second, we selected only those 3+/4+ cations whose ionic radii (r_A) produce a Goldschmidt tolerance factor[91] (t) greater than 0.71 (i.e., the stability limit of the perovskite structure), where:

$$t = \frac{r_A + r_B}{\sqrt{2}(r_B + r_O)} \tag{10}$$

r_B is the ionic radius of the six-fold-coordinated $B^{3+/2+}$, and r_O is the ionic radius of the six-fold-coordinated O^{2-} (1.40 Å). Note that t has a positivity rate of 74%, so even if the tolerance criterion predicts a perovskite structure to form, the composition still may not actually form. Recently, Bartel et al. developed a more accurate tolerance factor (positivity rate of 92%);[124] however, we use eq 10 because its solution is analytical and therefore easier to solve for the relevant range of r_B for which $t > 0.71$. That said, a numerical solution of the new tolerance factor[124] for r_B is not difficult to obtain and can be a strategy for subsequent studies. We selected only those compositions whose MP-PBE+*U*-calculated $E_{hull} \leq 0.025$ eV/atom: i.e., those that are predicted to be stable at room temperature. Table 1 gives the particularly promising candidates. $(La,Ce)^{3+}(Mn,Fe,Co)^{3+}O_3$ have been screened theoretically as candidates before by Emery et al.,[39] whereas those in Table 1 are new materials with known synthesis procedures. For example, $Bi(Fe,Co)O_3$ has a model E_v value in the target range of ≈3.4−3.9 (±0.1) eV for improved STCH materials.[7] Of these, $BiFeO_3$ is especially interesting because it is a promising multiferroic material with several synthesis routes already proven.[125] In addition, the absolute differences between the Bi^{3+} and Fe^{3+} V_r values ($|V_r[Bi^{3+} \rightarrow Bi^0] - V_r[Fe^{3+} \rightarrow Fe^{2+}]| = 0.46$ V vs O_2) and the Bi^{3+} and $Co^{8/3+}$ V_r values ($|V_r[Bi^{3+} \rightarrow Bi^0] - V_r[Co^{8/3+} \rightarrow Co^{2+}]| = 0.03$ V vs O_2) are small in comparison to that of the simultaneously redox-active Ce^{4+} and Mn^{3+} cations in Ca-, Ce-, and Mn-based ABO_3 perovskites ($|V_r[Ce^{4+} \rightarrow Ce^{3+}] - V_r[Mn^{3+} \rightarrow Mn^{2+}]| = 1.00$ V vs O_2).[7] Consequently, $Bi(Fe,Co)O_3$ might exhibit higher simultaneous redox activity and therefore a larger entropy of reduction. On the negative side, $BiFeO_3$ melts at a temperature (T_m) of 1234−1336 K, which is lower than a STCH cycle demands (≈2000 K). Encouragingly, the T_m values can be increased via Co doping,[126] so the quaternary species could prove sufficiently robust. Note that we list $YFeO_3$ as promising—despite its model E_v (4.76 eV) lying outside the target range (≈3.4−3.9 eV)—because its T_m value (1993 K) is greater than that of the E_v-ideal $Bi(Fe,Co)O_3$ (1234−1336 K) and therefore Y-doped $Bi(Fe,Co)O_3$ might be a promising candidate for STCH.

Finally, high-E_v metal oxides are optimal for semiconductors and ferroelectrics because their performance can be limited by the formation of deleterious defects. For example, V_Os induce ferroelectric domain wall pinning in $BiFeO_3$[127] (intermediate E_v) but not in $A^{2+}Ti^{4+}O_3$[36] (high E_v), which restricts polarization switching in the former. The most favorable B-site cations for high E_v include Ti^{4+}, Ti^{3+}, V^{3+}, and Cr^{3+}, which is consistent with the common ferroelectric crystals

https://doi.org/10.1021/jacs.1c05570
J. Am. Chem. Soc. 2021, 143, 13212−13227

$BaTiO_3$ and $PbTiO_3$[128] and those less explored, such as $CeCrO_3$[129] and $ScCrO_3$.[130]

Model Simplification. When quantum mechanics calculations are unavailable, E_b and V_r can be calculated from experimental[107−110] formation energies/enthalpies and element cohesive energies.[112] Moreover, E_g can be obtained from the experimental literature or computational databases[113,137−140] or by performing a simpler single-step self-consistent SCAN+U calculation. In cases where E_g is unknown or unreliable, we constructed simplified models for room-temperature-stable perovskites:

$$E_v = -1.8V_r - 66.0E_{hull} + 2.7 \quad (11)$$

and all perovskites:

$$E_v = 0.1\sum E_b - 1.7V_r - 6.5E_{hull} + 0.5 \quad (12)$$

with MAEs of 0.50 ± 0.05 and 0.74 ± 0.05 eV, respectively. Note that in eq 11 the estimated coefficient for $\sum E_b$ is −0.03 ± 0.15 eV and therefore fails to reject the null hypothesis. Figure S10 in the Supporting Information shows the performance of our simplified E_v models (eqs 11 and 12).

In scenarios where E_{hull} is undetermined or untrustworthy (e.g., for hypothetical and/or strongly correlated phases that are not present in computational materials databases such as MP, OQMD, and AFLOW), we suggest the following strategy when it is impractical to compute the phase diagram. First, one should use the model for stable perovskites in either Figure 3a (with E_g) or eq 11 (without E_g). If E_{hull} = 0.025 eV/atom, then $c_{hull}E_{hull}$ = −1.39 ± 0.40 and −1.65 ± 0.29 eV for the model with and without E_g, respectively. Therefore, if the perovskite is room-temperature-stable, then the maximum decrease in E_v is (1.39−1.65) ± 0.40 eV. Second, since stability often is desired, if the application-specific ideal-E_v range encompasses the model E_v value and the model E_v − 1.39 value (with E_g) or E_v − 1.65 value (without E_g), then the material is worth considering.

DISCUSSION

Comparison with a Prevailing Model. In the first part of the discussion, we compare our model to that of Deml et al.[66] (the state-of-the-art), which was trained on 45 insulating metal oxides, including binary and ternary main-group and transition-metal oxides in the antifluorite, corundum, rock salt, rutile, perovskite, and spinel structures. Note that both Deml et al. and we considered unstable metal oxides in our databases—58% (42%) of the metal oxides they (we) considered are room-temperature stable. Their model is:

$$E_v = 0.72\left[|\Delta H_f| + 0.60\left(E_{Op} + \frac{c_g}{2}E_g + 2.60\langle\Delta\chi\rangle\right)\right] - 2.07 \quad (13)$$

where ΔH_f is the metal oxide formation enthalpy in eV/atom, E_{Op} is the O 2p band center in eV, $\langle\Delta\chi\rangle$ is the average Pauling electronegativity difference between O^{2-} and its nearest cation neighbors, and c_g = 1.00 (1.50) for the GW-calculated (PBE+U-calculated) E_g in eV. Equation 13 has training and testing MAEs of 0.19−0.21 eV (the first value is for GW and the second is for PBE+U gaps) and 0.39 eV, respectively, where the latter is slightly better than our cross-validated MAE for room-temperature-stable materials (0.45 ± 0.04 eV). When it is normalized by the range of E_v, however, their testing MAE (9%) is slightly worse than ours (6−7%).

Despite the differences between some of the terms in our models, there is an underlying relationship between ΔH_f and V_r. To this end, consider the decomposition of binary M^{n+} oxides:

$$MO_{n/2} \rightarrow M + (n/4)O_2 \quad (14)$$

where the energy release upon decomposition is:

$$\Delta E_d = E_r[M^{n+} \rightarrow M^0] = -\Delta H_f \quad (15)$$

Inserting $E_r[M^{n+} \rightarrow M^0]$, n = 4, m = 0, and F into eq 5 yields:

$$V_r[M^{n+} \rightarrow M^0] = \frac{\Delta H_f}{nF} \quad (16)$$

Despite the direct mathematical relationship between ΔH_f and V_r, two important effects are better accounted for with the crystal V_r value used in our model than with ΔH_f. First, a neutral V_O reduces its neighboring cations; hence, the formation energy per reducing electron (V_r) provides a more consistent comparison across metal oxides with varied oxidation states. Second, ΔH_f neglects the presence of other stable nonzero oxidation states for the reduced metal, while the V_r value defined in our work better accounts for oxidation state changes. For example, $Ti^{4+} \rightarrow Ti^{3+}$ is more sensible than $Ti^{4+} \rightarrow Ti^0$ when $CaTiO_3$ is undergoing reduction because the V_O-induced two-electron reduction typically involves two or more cation acceptors rather than reduction of one cation all the way to its metallic state.

To provide a more quantitative comparison between our model and that of Deml et al.,[66] we fit a model (using training methods similar to those described in the Computational Methods) to their PBE+U-calculated E_v values with our descriptors. Note that $HgTiO_3$ was excluded from the reported model of Deml et al. and its inclusion increases the MAE from the reported 0.21 to 0.27 eV. Our model for their data, i.e.,

$$E_v = -1.2V_r + 0.3E_g + 1.87 \text{ eV} \quad (17)$$

highlights the important role of V_r in governing E_v trends, as it is one of only two metrics required to achieve MAE = 0.25 eV (see Figure 8). Notably, the coefficient we obtain for the E_g term (0.3) is similar to their model (0.22 or 0.32 depending on whether the PBE+U- or GW-based model is used), while the contribution of other descriptors used in their model drops down to a single V_r in ours. Additionally, our model is able to reproduce their PBE+U calculated E_v with lower errors and fewer parameters, highlighting that our descriptors are both more accurate and yield better physical insight.

Revisiting $HgTiO_3$, the authors in ref 66 hypothesize that its unpredictability (see the deviation between the orange marker with black outline and the dashed black line) "arises from the inadequate treatment of the filled Hg d orbitals in DFT". Our results show, however, that the inclusion of V_r in the model enables a better prediction (AE = 0.45 eV vs 2.10 eV for our model vs their model, respectively) of the PBE+U-calculated E_v value for $HgTiO_3$ (3.05 eV). This improvement can be ascribed to the greater reducibility and therefore control over the E_v value of Hg^{2+} (MP-PBE+U-calculated $V_r[Hg^{2+} \rightarrow Hg^0]$ = −0.65 V vs O_2) relative to Ti^{4+} (MP-PBE+U-calculated $V_r[Ti^{4+} \rightarrow Ti^{3+}]$ = −2.25 V vs O_2), which is captured by V_r but not by a combination of ΔH_f, E_{Op}, E_g, and $\Delta\chi$.

Avenues for Improving and Extending the Model. In the second part of the discussion, we first analyze the six outliers in Figure 3b. On the basis of our low-, intermediate-,

https://doi.org/10.1021/jacs.1c05570
J. Am. Chem. Soc. 2021, 143, 13212−13227

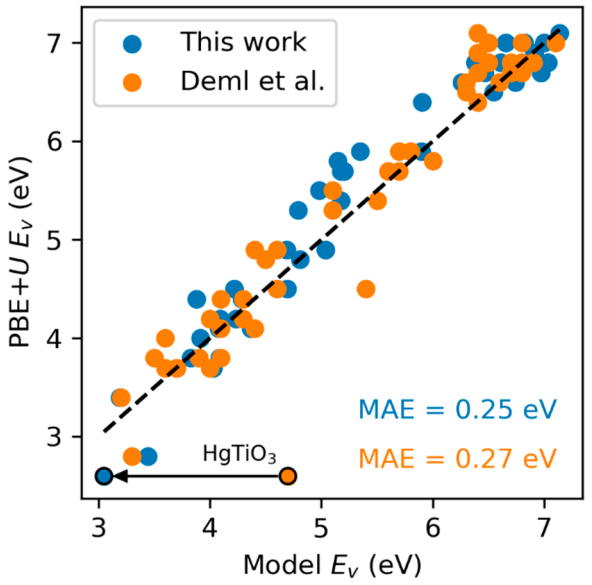

Figure 8. Comparison of our model with the prevailing model in the literature.[66]

and high-E_v bins, we classify these outliers as either quantitative (where the SCAN+U-calculated and model-predicted E_v values are in the same bin) or qualitative (where these E_v values are in different bins). The quantitative outliers are monoclinic (m-)$LaCrO_3$ ($P2_1/c$) and hexagonal (h-)$CaTiO_3$ ($P6_3/mmc$), whereas the qualitative outliers are rhombohedral (r-)$BaCrO_3$ ($R\bar{3}c$), tetragonal (t-)$LaCoO_3$ ($P4mm$), cubic (c-)$LaCoO_3$ ($Pm\bar{3}m$, ICSD #28921), and c-$LaTiO_3$ ($Pm\bar{3}m$, ICSD #28908). In general, multiple possible reasons exist for deviations in the SCAN+U-calculated and model-predicted E_v values. First, the intrinsic instability (E_{hull} > 0.042 eV/atom for all six outliers) may catalyze nonlocal changes in the structure that models with local features cannot capture. That said, given the small number of outliers, E_{hull} captures most of the stability-related contributions to E_v. Second, for simplicity in the screening process, we aligned ferromagnetically the magnetic moments of all cations. Despite this approximation leading to a good description of many basic properties of standard ferromagnetic materials, such as permanent magnetic moments and phase diagrams,[141] antiferromagnetism, relevant for the Cr-containing outliers, may lead to inconsistencies between the initial and final spin configurations. Finally, although we considered the high-, intermediate-, and low-spin states for the Co-containing outliers, a more comprehensive analysis of their magnetic structures is left for future work.

Next, we outline avenues for improving the model. One limitation of the model is using E_b from binary systems, as the actual bond lengths in ternary perovskites (and beyond) structures may be significantly different from the binary oxide bond lengths. So, to account for this, one could either do more calculations to see how E_b changes with bond length for individual systems or fit a simple function (e.g., an exponent or a Gaussian centered around the binary metal oxide bond length) as a weighting factor. In any case, modifying E_b should lead to small improvements in the MAE of models since c_b is quite small.

With respect to the dependence of E_v on V_r, our ideas for refining the model are motivated by the fact that the cross-validated c_r value can be understood as the number of electrons (N_e) donated by an O^{2-} to its most reducible cation neighbors upon V_O formation. Moreover, N_e being approximately equal to 1.5 (see Figure 3a) and not 2 is related to how the cation-reduction energy cost for creating V_Os gets split. V_r contributes about 75−80% of the cost, whereas ∼15% of the cost is accounted for by E_g (which captures crystal field effects and any delocalization of electrons upon V_O formation); this combination is why $c_r + c_g$ adds up to 1.9. We hypothesize that the 10% remaining contribution comes from stability and bond-dissociation effects (where ions that do not undergo reduction can contribute). To explore further the role of electron delocalization in determining the c_r/c_g split across a wider range of the chemical phase space, one could calculate E_v for electronically diverse compounds whose anions neighbor O in the periodic table, such as metallic transition-metal phosphides for electrocatalysis,[142−144] semiconducting chalcogenides (sulfides and selenides for solar energy conversion),[145−147] and hybrid organic-inorganic metal halides (e.g., for optoelectronics).[148−150]

Finally, now we summarize some opportunities for extending the model by exploring other materials classes, including defect-defect interactions, and studying other defect types. First, we recommend testing (and, if necessary, retraining) the model on non-perovskite and non-ternary oxides. Second, for achievable V_O concentrations, defect-defect interactions may be non-negligible, thereby requiring the development of schemes to capture changes, for example, in the electrostatic repulsion between reduced and descreened cations and vacancy-vacancy interactions. Finally, we suggest that this approach be extended to other defect types such as bulk cation vacancies (which, e.g., affect the performance of LSCF cathodes for SOFCs[151]), charged vacancies and their transition levels (which, e.g., induce nonradiative recombination of photoexcited charge carriers in kesterite solar cells[152] and ABO_3 perovskites[153]), and surface vacancies (which, e.g., alter the electrical properties of SnO_2 gas sensors[154]).

CONCLUSIONS

Metal oxide perovskites have received intense scrutiny for clean energy and computer memory applications due to their flexible structure, stability, wide composition space, and mixed ionic electronic conductivity. While exciting progress continues, a simple phenomenological explanation for the trends in oxygen vacancy (V_O) formation energies (E_v), which play a critical role in determining the performance of perovskite metal-oxide-based devices, has remained elusive. Here, we have introduced a machine-learned linear model that is based on E_v values of ABO_3 perovskites, where A = Ca, Sr, Ba, La, Ce and B = Ti, V, Cr, Mn, Fe, Co, Ni, in six lattice systems (monoclinic, orthorhombic, tetragonal, rhombohedral, hexagonal, and cubic). The model takes as inputs crystal bond dissociation energies, crystal reduction potentials, band gaps, and energies above the convex hull, which one can obtain from theoretical or experimental databases. Notably, we have devised crystal bond dissociation energies and crystal reduction potentials as the solid-state variants of their molecular and aqueous electrochemistry analogues, respectively, to systematically improve the description of bond dissociation and reduction of multivalent cations in solids. Additionally, we demonstrate that the model can be simplified, with acceptable losses in accuracy, such that only crystal bond dissociation energies and crystal reduction potentials are needed in scenarios where band gaps and energies above the convex hull are difficult to

https://doi.org/10.1021/jacs.1c05570
J. Am. Chem. Soc. 2021, 143, 13212−13227

estimate. Also, we predict $BiFeO_3$ and $BiCoO_3$ or a mixture might be viable candidates for solar thermochemical water and/or carbon dioxide splitting applications (intermediate E_v, if the melting point can be pushed high enough: e.g., via Y-doping), with $CeCrO_3$ and $ScCrO_3$ as possible V_O-resistant ferroelectrics (high E_v), indicating the effect that our model can make in materials discovery. Adding further credibility to our model is our rediscovery of Co-based perovskites as robust solid oxide fuel cell cathodes (low E_v). Finally, we present our perspectives on how to improve and extend the model, which already provides both accurate and efficient predictions for high-throughput screening and an intuitive and modular phenomenology for applications to metal oxide perovskites and beyond.

■ ASSOCIATED CONTENT

Supporting Information

The Supporting Information is available free of charge at https://pubs.acs.org/doi/10.1021/jacs.1c05570.

Further details about the distribution of ABO_3 perovskite structures, distribution of neutral oxygen vacancy formation energies, convergence of oxygen vacancy formation energies in different crystal systems with respect to supercell size, distribution of energies above the convex hull, periodic trends in experimental cohesive energies, cell-size convergence of total energies for neutral atoms in their electronic ground states, theoretical and experimental cohesive energies across all metal oxides considered, correlation of experimental bond dissociation energies for neutral diatomic molecules and diatomic cations with respect to SCAN+*U*-calculated crystal bond dissociation energies, specific trends in the SCAN+*U*-calculated and experimental crystal reduction potentials, and SCAN+*U*-calculated vs simplified-model-predicted oxygen vacancy formation energies (PDF)

Comma-separated-value files containing crystal structures, total energies, magnetic moments, charges, band gaps, and crystal features for all systems considered (ZIP)

■ AUTHOR INFORMATION

Corresponding Author

Emily A. Carter − *Department of Mechanical and Aerospace Engineering, Princeton University, Princeton, New Jersey 08544-5263, United States; Office of the Chancellor and Department of Chemical and Biomolecular Engineering, University of California, Los Angeles, Los Angeles, California 90095, United States;* orcid.org/0000-0001-7330-7554; Email: eac@princeton.edu, eac@ucla.edu

Authors

Robert B. Wexler − *Department of Mechanical and Aerospace Engineering, Princeton University, Princeton, New Jersey 08544-5263, United States;* orcid.org/0000-0002-6861-6421

Gopalakrishnan Sai Gautam − *Department of Mechanical and Aerospace Engineering, Princeton University, Princeton, New Jersey 08544-5263, United States;* Present Address: Department of Materials Engineering, Indian Institute of Science, Bengaluru, Karnataka 560012, India; orcid.org/0000-0002-1303-0976

Ellen B. Stechel − *ASU LightWorks and the School of Molecular Sciences, Arizona State University, Tempe, Arizona 85287-5402, United States;* orcid.org/0000-0002-5379-2908

Complete contact information is available at: https://pubs.acs.org/10.1021/jacs.1c05570

Notes

The authors declare no competing financial interest.

■ ACKNOWLEDGMENTS

The authors gratefully acknowledge research support from the HydroGEN Advanced Water Splitting Materials Consortium, established as part of the Energy Materials Network under the U.S. Department of Energy, Office of Energy Efficiency and Renewable Energy, Fuel Cell Technologies Office, under Award Number DE-EE0008090. The authors also acknowledge the computational resources sponsored by the Department of Energy's Office of Energy Efficiency and Renewable Energy located at the National Renewable Energy Laboratory. The authors also thank Princeton University for computing resources. The views and opinions of the authors expressed herein do not necessarily state or reflect those of the United States Government or any agency thereof. Neither the United States Government nor any agency thereof, nor any of their employees, makes any warranty, expressed or implied, or assumes any legal liability or responsibility for the accuracy, completeness, or usefulness of any information, apparatus, product, or process disclosed, or represents that its use would not infringe privately owned rights.

■ REFERENCES

(1) Scheffe, J. R.; Weibel, D.; Steinfeld, A. Lanthanum-Strontium-Manganese Perovskites as Redox Materials for Solar Thermochemical Splitting of H_2O and CO_2. *Energy Fuels* **2013**, *27* (8), 4250−4257.

(2) Demont, A.; Abanades, S.; Beche, E. Investigation of Perovskite Structures as Oxygen-Exchange Redox Materials for Hydrogen Production from Thermochemical Two-Step Water-Splitting Cycles. *J. Phys. Chem. C* **2014**, *118* (24), 12682−12692.

(3) Orfila, M.; Linares, M.; Molina, R.; Botas, J. Á.; Sanz, R.; Marugán, J. Perovskite Materials for Hydrogen Production by Thermochemical Water Splitting. *Int. J. Hydrogen Energy* **2016**, *41* (42), 19329−19338.

(4) Steinfeld, A. Solar Thermochemical Production of Hydrogen - A Review. *Sol. Energy* **2005**, *78* (5), 603−615.

(5) Turner, J.; Sverdrup, G.; Mann, M. K.; Maness, P.-C.; Kroposki, B.; Ghirardi, M.; Evans, R. J.; Blake, D. Renewable Hydrogen Production. *Int. J. Energy Res.* **2008**, *32* (5), 379−407.

(6) Steinfeld, A. Solar Hydrogen Production via a Two-Step Water-Splitting Thermochemical Cycle Based on Zn/ZnO Redox Reactions. *Int. J. Hydrogen Energy* **2002**, *27* (6), 611−619.

(7) Sai Gautam, G.; Stechel, E. B.; Carter, E. A. Exploring Ca-Ce-M-O (M = 3d Transition Metal) Oxide Perovskites for Solar Thermochemical Applications. *Chem. Mater.* **2020**, *32*, 9964.

(8) Mastronardo, E.; Qian, X.; Coronado, J. M.; Haile, S. Fe-Doped $CaMnO_3$ for Thermochemical Heat Storage Application. *AIP Conf. Proc.* **2018**, *2126*, 210005.

(9) Imponenti, L.; Albrecht, K. J.; Kharait, R.; Sanders, M. D.; Jackson, G. S. Redox Cycles with Doped Calcium Manganites for Thermochemical Energy Storage to 1000 °C. *Appl. Energy* **2018**, *230* (April), 1−18.

(10) Babiniec, S. M.; Coker, E. N.; Miller, J. E.; Ambrosini, A. Doped Calcium Manganites for Advanced High-Temperature Thermochemical Energy Storage. *Int. J. Energy Res.* **2016**, *40* (2), 280−284.

(11) Zhang, Z.; Andre, L.; Abanades, S. Experimental Assessment of Oxygen Exchange Capacity and Thermochemical Redox Cycle Behavior of Ba and Sr Series Perovskites for Solar Energy Storage. *Sol. Energy* **2016**, *134*, 494−502.
(12) Ermanoski, I.; Stechel, E. B. Thermally-Driven Adsorption/Desorption Cycle for Oxygen Pumping in Thermochemical Fuel Production. *Sol. Energy* **2020**, *198*, 578−585.
(13) Brendelberger, S.; Vieten, J.; Roeb, M.; Sattler, C. Thermochemical Oxygen Pumping for Improved Hydrogen Production in Solar Redox Cycles. *Int. J. Hydrogen Energy* **2019**, *44* (20), 9802−9810.
(14) Vieten, J.; Bulfin, B.; Starr, D. E.; Hariki, A.; de Groot, F. M. F.; Azarpira, A.; Zachäus, C.; Hävecker, M.; Skorupska, K.; Knoblauch, N.; Schmücker, M.; Roeb, M.; Sattler, C. Redox Behavior of Solid Solutions in the $SrFe_{1-x}Cu_xO_{3-\delta}$ System for Application in Thermochemical Oxygen Storage and Air Separation. *Energy Technol.* **2019**, *7* (1), 131−139.
(15) Bush, H. E.; Datta, R.; Loutzenhiser, P. G. Aluminum-Doped Strontium Ferrites for a Two-Step Solar Thermochemical Air Separation Cycle: Thermodynamic Characterization and Cycle Analysis. *Sol. Energy* **2019**, *188* (June), 775−786.
(16) Krzystowczyk, E.; Wang, X.; Dou, J.; Haribal, V.; Li, F. Substituted $SrFeO_3$ as Robust Oxygen Sorbents for Thermochemical Air Separation: Correlating Redox Performance with Compositional and Structural Properties. *Phys. Chem. Chem. Phys.* **2020**, *22* (16), 8924−8932.
(17) Farr, T. P.; Nguyen, N. P.; Bush, H. E.; Ambrosini, A.; Loutzenhiser, P. G. An A- and B-Site Substitutional Study of $SrFeO_{3-\delta}$ Perovskites for Solar Thermochemical Air Separation. *Materials* **2020**, *13* (22), 5123.
(18) Ezbiri, M.; Allen, K. M.; Gàlvez, M. E.; Michalsky, R.; Steinfeld, A. Design Principles of Perovskites for Thermochemical Oxygen Separation. *ChemSusChem* **2015**, *8* (11), 1966−1971.
(19) Adler, S. B. Factors Governing Oxygen Reduction in Solid Oxide Fuel Cell Cathodes. *Chem. Rev.* **2004**, *104* (10), 4791−4844.
(20) Kharton, V. V.; Marques, F. M. B.; Atkinson, A. Transport Properties of Solid Oxide Electrolyte Ceramics: A Brief Review. *Solid State Ionics* **2004**, *174* (1−4), 135−149.
(21) Malavasi, L.; Fisher, C. A. J.; Islam, M. S. Oxide-Ion and Proton Conducting Electrolyte Materials for Clean Energy Applications: Structural and Mechanistic Features. *Chem. Soc. Rev.* **2010**, *39* (11), 4370.
(22) Muñoz-García, A. B.; Ritzmann, A. M.; Pavone, M.; Keith, J. A.; Carter, E. A. Oxygen Transport in Perovskite-Type Solid Oxide Fuel Cell Materials: Insights from Quantum Mechanics. *Acc. Chem. Res.* **2014**, *47* (11), 3340−3348.
(23) Pavone, M.; Ritzmann, A. M.; Carter, E. A. Quantum-Mechanics-Based Design Principles for Solid Oxide Fuel Cell Cathode Materials. *Energy Environ. Sci.* **2011**, *4* (12), 4933−4937.
(24) Mogensen, M.; Lybye, D.; Bonanos, N.; Hendriksen, P. V.; Poulsen, F. W. Factors Controlling the Oxide Ion Conductivity of Fluorite and Perovskite Structured Oxides. *Solid State Ionics* **2004**, *174* (1−4), 279−286.
(25) Wachs, I. E.; Routray, K. Catalysis Science of Bulk Mixed Oxides. *ACS Catal.* **2012**, *2* (6), 1235−1246.
(26) Aguadero, A.; Pérez-Coll, D.; Alonso, J. A.; Skinner, S. J.; Kilner, J. A New Family of Mo-Doped $SrCoO_{3-\delta}$ Perovskites for Application in Reversible Solid State Electrochemical Cells. *Chem. Mater.* **2012**, *24* (14), 2655−2663.
(27) Gajek, M.; Bibes, M.; Fusil, S.; Bouzehouane, K.; Fontcuberta, J.; Barthélémy, A.; Fert, A. Tunnel Junctions with Multiferroic Barriers. *Nat. Mater.* **2007**, *6* (4), 296−302.
(28) Chanthbouala, A.; Crassous, A.; Garcia, V.; Bouzehouane, K.; Fusil, S.; Moya, X.; Allibe, J.; Dlubak, B.; Grollier, J.; Xavier, S.; Deranlot, C.; Moshar, A.; Proksch, R.; Mathur, N. D.; Bibes, M.; Barthélémy, A. Solid-State Memories Based on Ferroelectric Tunnel Junctions. *Nat. Nanotechnol.* **2012**, *7* (2), 101−104.
(29) Scott, J. F. Device Physics of Ferroelectric Memories. *Ferroelectrics* **1996**, *183* (1), 51−63.
(30) Meng, Q.-L.; Lee, C.; Shigeta, S.; Kaneko, H.; Tamaura, Y. Solar Hydrogen Production Using $Ce_{1-x}Li_xO_{2-\delta}$ Solid Solutions via a Thermochemical, Two-Step Water-Splitting Cycle. *J. Solid State Chem.* **2012**, *194*, 343−351.
(31) Bayon, A.; de la Calle, A.; Ghose, K. K.; Page, A.; McNaughton, R. Experimental, Computational and Thermodynamic Studies in Perovskites Metal Oxides for Thermochemical Fuel Production: A Review. *Int. J. Hydrogen Energy* **2020**, *45* (23), 12653−12679.
(32) Steele, B. C. H. Oxygen Transport and Exchange in Oxide Ceramics. *J. Power Sources* **1994**, *49* (1−3), 1−14.
(33) Lee, Y.-L.; Kleis, J.; Rossmeisl, J.; Shao-Horn, Y.; Morgan, D. Prediction of Solid Oxide Fuel Cell Cathode Activity with First-Principles Descriptors. *Energy Environ. Sci.* **2011**, *4* (10), 3966.
(34) Ioffe, L. B.; Vinokur, V. M. Dynamics of Interfaces and Dislocations in Disordered Media. *J. Phys. C: Solid State Phys.* **1987**, *20* (36), 6149−6158.
(35) Chauve, P.; Giamarchi, T.; Le Doussal, P. Creep and Depinning in Disordered Media. *Phys. Rev. B: Condens. Matter Mater. Phys.* **2000**, *62* (10), 6241−6267.
(36) Liu, S.; Grinberg, I.; Rappe, A. M. Intrinsic Ferroelectric Switching from First Principles. *Nature* **2016**, *534* (7607), 360−363.
(37) Nelson, C. T.; Gao, P.; Jokisaari, J. R.; Heikes, C.; Adamo, C.; Melville, A.; Baek, S.-H.; Folkman, C. M.; Winchester, B.; Gu, Y.; Liu, Y.; Zhang, K.; Wang, E.; Li, J.; Chen, L.-Q.; Eom, C.-B.; Schlom, D. G.; Pan, X. Domain Dynamics During Ferroelectric Switching. *Science (Washington, DC, U. S.)* **2011**, *334* (6058), 968−971.
(38) Ermanoski, I.; Siegel, N. P.; Stechel, E. B. A New Reactor Concept for Efficient Solar-Thermochemical Fuel Production. *J. Sol. Energy Eng.* **2013**, *135* (3), 1−10.
(39) Emery, A. A.; Saal, J. E.; Kirklin, S.; Hegde, V. I.; Wolverton, C. High-Throughput Computational Screening of Perovskites for Thermochemical Water Splitting Applications. *Chem. Mater.* **2016**, *28* (16), 5621−5634.
(40) Meredig, B.; Wolverton, C. First-Principles Thermodynamic Framework for the Evaluation of Thermochemical H_2O- or CO_2-Splitting Materials. *Phys. Rev. B: Condens. Matter Mater. Phys.* **2009**, *80* (24), 245119.
(41) Mayeshiba, T. T.; Morgan, D. D. Factors Controlling Oxygen Migration Barriers in Perovskites. *Solid State Ionics* **2016**, *296*, 71−77.
(42) Ritzmann, A. M.; Muñoz-García, A. B.; Pavone, M.; Keith, J. A.; Carter, E. A. Ab Initio DFT+U Analysis of Oxygen Vacancy Formation and Migration in $La_{1-x}Sr_xFeO_{3-\delta}$ (x = 0, 0.25, 0.50). *Chem. Mater.* **2013**, *25* (15), 3011−3019.
(43) Pavone, M.; Muñoz-García, A. B.; Ritzmann, A. M.; Carter, E. A. First-Principles Study of Lanthanum Strontium Manganite: Insights into Electronic Structure and Oxygen Vacancy Formation. *J. Phys. Chem. C* **2014**, *118* (25), 13346−13356.
(44) Mizusaki, J.; Sasamoto, T.; Cannon, W. R.; Bowen, H. K. Electronic Conductivity, Seebeck Coefficient, and Defect Structure of $La_{1-x}Sr_xFeO_3$ (X = 0.1, 0.25). *J. Am. Ceram. Soc.* **1983**, *66* (4), 247−252.
(45) Muñoz-García, A. B.; Pavone, M.; Carter, E. A. Effect of Antisite Defects on the Formation of Oxygen Vacancies in Sr_2FeMoO_6: Implications for Ion and Electron Transport. *Chem. Mater.* **2011**, *23* (20), 4525−4536.
(46) Muñoz-García, A. B.; Bugaris, D. E.; Pavone, M.; Hodges, J. P.; Huq, A.; Chen, F.; zur Loye, H.-C.; Carter, E. A. Unveiling Structure-Property Relationships in $Sr_2Fe_{1.5}Mo_{0.5}O_{6-\delta}$, an Electrode Material for Symmetric Solid Oxide Fuel Cells. *J. Am. Chem. Soc.* **2012**, *134* (15), 6826−6833.
(47) Muñoz-García, A. B.; Pavone, M.; Ritzmann, A. M.; Carter, E. A. Oxide Ion Transport in $Sr_2Fe_{1.5}Mo_{0.5}O_{6-\delta}$, a Mixed Ion-Electron Conductor: New Insights from First Principles Modeling. *Phys. Chem. Chem. Phys.* **2013**, *15* (17), 6250.
(48) Walsh, A.; Scanlon, D. O. Polymorphism of Indium Oxide: Materials Physics of Orthorhombic In_2O_3. *Phys. Rev. B: Condens. Matter Mater. Phys.* **2013**, *88* (16), 161201.

https://doi.org/10.1021/jacs.1c05570
J. Am. Chem. Soc. 2021, 143, 13212−13227

(49) Shandalov, M.; McIntyre, P. C. Size-Dependent Polymorphism in HfO_2 Nanotubes and Nanoscale Thin Films. *J. Appl. Phys.* **2009**, *106* (8), 084322.
(50) Park, M. H.; Lee, D. H.; Yang, K.; Park, J.-Y.; Yu, G. T.; Park, H. W.; Materano, M.; Mittmann, T.; Lomenzo, P. D.; Mikolajick, T.; Schroeder, U.; Hwang, C. S. Review of Defect Chemistry in Fluorite-Structure Ferroelectrics for Future Electronic Devices. *J. Mater. Chem. C* **2020**, *8* (31), 10526−10550.
(51) Chen, C.; Ciucci, F. Designing Fe-Based Oxygen Catalysts by Density Functional Theory Calculations. *Chem. Mater.* **2016**, *28* (19), 7058−7065.
(52) Maiti, D.; Hare, B. J.; Daza, Y. A.; Ramos, A. E.; Kuhn, J. N.; Bhethanabotla, V. R. Earth Abundant Perovskite Oxides for Low Temperature CO_2 Conversion. *Energy Environ. Sci.* **2018**, *11* (3), 648−659.
(53) Hinuma, Y.; Toyao, T.; Kamachi, T.; Maeno, Z.; Takakusagi, S.; Furukawa, S.; Takigawa, I.; Shimizu, K. Density Functional Theory Calculations of Oxygen Vacancy Formation and Subsequent Molecular Adsorption on Oxide Surfaces. *J. Phys. Chem. C* **2018**, *122* (51), 29435−29444.
(54) Helali, Z.; Jedidi, A.; Syzgantseva, O. A.; Calatayud, M.; Minot, C. Scaling Reducibility of Metal Oxides. *Theor. Chem. Acc.* **2017**, *136* (9), 100.
(55) Carey, J. J.; Nolan, M. Enhancing the Oxygen Vacancy Formation and Migration in Bulk Chromium(III) Oxide by Alkali Metal Doping: A Change from Isotropic to Anisotropic Oxygen Diffusion. *J. Mater. Chem. A* **2017**, *5* (30), 15613−15630.
(56) Scaranto, J.; Idriss, H. The Effect of Uranium Cations on the Redox Properties of CeO_2 Within the Context of Hydrogen Production from Water. *Top. Catal.* **2015**, *58* (2−3), 143−148.
(57) Zheng, Y.-S.; Zhang, M.; Li, Q.; Zhu, Y.-A.; Sui, Z.-J.; Chen, D.; Zhou, X.-G. Electronic Origin of Oxygen Transport Behavior in La-Based Perovskites: A Density Functional Theory Study. *J. Phys. Chem. C* **2019**, *123* (1), 275−290.
(58) Yamamoto, T.; Mizoguchi, T. First Principles Study on Oxygen Vacancy Formation in Rock Salt-Type Oxides MO (M: Mg, Ca, Sr and Ba). *Ceram. Int.* **2013**, *39*, S287−S292.
(59) Dou, J.; Krzystowczyk, E.; Wang, X.; Robbins, T.; Ma, L.; Liu, X.; Li, F. A- and B-site Codoped $SrFeO_3$ Oxygen Sorbents for Enhanced Chemical Looping Air Separation. *ChemSusChem* **2020**, *13* (2), 385−393.
(60) Ritzmann, A. M.; Dieterich, J. M.; Carter, E. A. Density Functional Theory + U Analysis of the Electronic Structure and Defect Chemistry of LSCF ($La_{0.5}Sr_{0.5}Co_{0.25}Fe_{0.75}O_{3-\delta}$). *Phys. Chem. Chem. Phys.* **2016**, *18* (17), 12260−12269.
(61) Deml, A. M.; Stevanović, V.; Muhich, C. L.; Musgrave, C. B.; O'Hayre, R. Oxide Enthalpy of Formation and Band Gap Energy as Accurate Descriptors of Oxygen Vacancy Formation Energetics. *Energy Environ. Sci.* **2014**, *7* (6), 1996.
(62) Choi, M.; Ibrahim, I. A. M.; Kim, K.; Koo, J. Y.; Kim, S. J.; Son, J.-W.; Han, J. W.; Lee, W. Engineering of Charged Defects at Perovskite Oxide Surfaces for Exceptionally Stable Solid Oxide Fuel Cell Electrodes. *ACS Appl. Mater. Interfaces* **2020**, *12* (19), 21494−21504.
(63) Akhade, S. A.; Kitchin, J. R. Effects of Strain, d-Band Filling, and Oxidation State on the Surface Electronic Structure and Reactivity of 3d Perovskite Surfaces. *J. Chem. Phys.* **2012**, *137* (8), 084703.
(64) Deml, A. M.; Stevanović, V.; Holder, A. M.; Sanders, M.; O'Hayre, R.; Musgrave, C. B. Tunable Oxygen Vacancy Formation Energetics in the Complex Perovskite Oxide $Sr_xLa_{1-x}Mn_yAl_{1-y}O_3$. *Chem. Mater.* **2014**, *26* (22), 6595−6602.
(65) Xie, W.; Lee, Y.-L.; Shao-Horn, Y.; Morgan, D. Oxygen Point Defect Chemistry in Ruddlesden-Popper Oxides $(La_{1-x}Sr_x)_2MO_{4\pm\delta}$ (M = Co, Ni, Cu). *J. Phys. Chem. Lett.* **2016**, *7* (10), 1939−1944.
(66) Deml, A. M.; Holder, A. M.; O'Hayre, R. P.; Musgrave, C. B.; Stevanović, V. Intrinsic Material Properties Dictating Oxygen Vacancy Formation Energetics in Metal Oxides. *J. Phys. Chem. Lett.* **2015**, *6* (10), 1948−1953.
(67) Migani, A.; Vayssilov, G. N.; Bromley, S. T.; Illas, F.; Neyman, K. M. Dramatic Reduction of the Oxygen Vacancy Formation Energy in Ceria Particles: A Possible Key to Their Remarkable Reactivity at the Nanoscale. *J. Mater. Chem.* **2010**, *20* (46), 10535.
(68) Krcha, M. D.; Mayernick, A. D.; Janik, M. J. Periodic Trends of Oxygen Vacancy Formation and C-H Bond Activation over Transition Metal-Doped CeO_2(111) Surfaces. *J. Catal.* **2012**, *293*, 103−115.
(69) Li, B.; Metiu, H. DFT Studies of Oxygen Vacancies on Undoped and Doped La_2O_3 Surfaces. *J. Phys. Chem. C* **2010**, *114* (28), 12234−12244.
(70) Perdew, J. P.; Burke, K.; Ernzerhof, M. Generalized Gradient Approximation Made Simple. *Phys. Rev. Lett.* **1996**, *77* (18), 3865−3868.
(71) Wang, L.; Maxisch, T.; Ceder, G. Oxidation Energies of Transition Metal Oxides within the GGA+U Framework. *Phys. Rev. B: Condens. Matter Mater. Phys.* **2006**, *73* (19), 195107.
(72) Sun, J.; Ruzsinszky, A.; Perdew, J. Strongly Constrained and Appropriately Normed Semilocal Density Functional. *Phys. Rev. Lett.* **2015**, *115* (3), 036402.
(73) Sun, J.; Remsing, R. C.; Zhang, Y.; Sun, Z.; Ruzsinszky, A.; Peng, H.; Yang, Z.; Paul, A.; Waghmare, U.; Wu, X.; Klein, M. L.; Perdew, J. P. Accurate First-Principles Structures and Energies of Diversely Bonded Systems from an Efficient Density Functional. *Nat. Chem.* **2016**, *8* (9), 831−836.
(74) Anisimov, V. I.; Zaanen, J.; Andersen, O. K. Band Theory and Mott Insulators: Hubbard U Instead of Stoner I. *Phys. Rev. B: Condens. Matter Mater. Phys.* **1991**, *44* (3), 943−954.
(75) Liechtenstein, A. I.; Anisimov, V. I.; Zaanen, J. Density-Functional Theory and Strong Interactions: Orbital Ordering in Mott-Hubbard Insulators. *Phys. Rev. B: Condens. Matter Mater. Phys.* **1995**, *52* (8), R5467−R5470.
(76) Anisimov, V. I.; Aryasetiawan, F.; Lichtenstein, A. I. First-Principles Calculations of the Electronic Structure and Spectra of Strongly Correlated Systems: The LDA + U Method. *J. Phys.: Condens. Matter* **1997**, *9* (4), 767−808.
(77) Sai Gautam, G.; Carter, E. A. Evaluating Transition Metal Oxides within DFT-SCAN and SCAN+U Frameworks for Solar Thermochemical Applications. *Phys. Rev. Mater.* **2018**, *2* (9), 095401.
(78) Long, O. Y.; Sai Gautam, G.; Carter, E. A. Evaluating Optimal U for 3d Transition-Metal Oxides within the SCAN+U Framework. *Phys. Rev. Mater.* **2020**, *4* (4), 045401.
(79) Qi, Y.; Liu, S.; Grinberg, I.; Rappe, A. M. Atomistic Description for Temperature-Driven Phase Transitions in $BaTiO_3$. *Phys. Rev. B: Condens. Matter Mater. Phys.* **2016**, *94* (13), 134308.
(80) Wexler, R. B.; Qi, Y.; Rappe, A. M. Sr-Induced Dipole Scatter in $Ba_xSr_{1-x}TiO_3$: Insights from a Transferable-Bond Valence-Based Interatomic Potential. *Phys. Rev. B* **2019**, *100*, 174109.
(81) Liu, S.; Grinberg, I.; Rappe, A. M. Development of a Bond-Valence Based Interatomic Potential for $BiFeO_3$ for Accurate Molecular Dynamics Simulations. *J. Phys.: Condens. Matter* **2013**, *25* (10), 102202.
(82) Kresse, G.; Hafner, J. Ab Initio Molecular Dynamics for Liquid Metals. *Phys. Rev. B: Condens. Matter Mater. Phys.* **1993**, *47* (1), 558−561.
(83) Kresse, G.; Furthmüller, J. Efficient Iterative Schemes for Ab Initio Total-Energy Calculations Using a Plane-Wave Basis Set. *Phys. Rev. B: Condens. Matter Mater. Phys.* **1996**, *54* (16), 11169−11186.
(84) Dudarev, S. L.; Botton, G. A.; Savrasov, S. Y.; Humphreys, C. J.; Sutton, A. P. Electron-Energy-Loss Spectra and the Structural Stability of Nickel Oxide: An LSDA+U Study. *Phys. Rev. B: Condens. Matter Mater. Phys.* **1998**, *57* (3), 1505−1509.
(85) Blöchl, P. E. Projector Augmented-Wave Method. *Phys. Rev. B: Condens. Matter Mater. Phys.* **1994**, *50* (24), 17953−17979.
(86) Kresse, G.; Joubert, D. From Ultrasoft Pseudopotentials to the Projector Augmented-Wave Method. *Phys. Rev. B: Condens. Matter Mater. Phys.* **1999**, *59* (3), 1758−1775.
(87) Sai Gautam, G.; Stechel, E. B.; Carter, E. A. A First-Principles-Based Sub-Lattice Formalism for Predicting Off-Stoichiometry in

Materials for Solar Thermochemical Applications: The Example of Ceria. *Adv. Theory Simulations* **2020**, *3*, 2000112.
(88) Monkhorst, H. J.; Pack, J. D. Special Points for Brillouin-Zone Integrations. *Phys. Rev. B* **1976**, *13* (12), 5188−5192.
(89) Ritzmann, A. M. *First Principles Insights Into Oxygen Transport in Solid Oxide Fuel Cell Cathode Materials Based on Lanthanum Strontium Cobalt Ferrite*; Princeton University: 2016.
(90) Curnan, M. T.; Kitchin, J. R. Effects of Concentration, Crystal Structure, Magnetism, and Electronic Structure Method on First-Principles Oxygen Vacancy Formation Energy Trends in Perovskites. *J. Phys. Chem. C* **2014**, *118* (49), 28776−28790.
(91) Goldschmidt, V. M. The Principles of Distribution of Chemical Elements in Minerals and Rocks. The Seventh Hugo Müller Lecture, Delivered before the Chemical Society on March 17th, 1937. *J. Chem. Soc.* **1937**, *0*, 655−673.
(92) Wexler, R. B.; Sai Gautam, G.; Carter, E. A. Exchange-Correlation Functional Challenges in Modeling Quaternary Chalcogenides. *Phys. Rev. B* **2020**, *102* (5), 054101.
(93) Burzlaff, H.; Zimmermann, H. Point-Group Symbols. In *International Tables for Crystallography*; International Union of Crystallography: Chester, England, 2006; pp 818−820. DOI: 10.1107/97809553602060000524.
(94) Bergerhoff, G.; Brown, I. D. Inorganic Crystal Structure Database. *Acta Crystallogr. Sect. A Found. Crystallogr.* **1981**, 1.
(95) Togo, A.; Tanaka, I. Spglib: A Software Library for Crystal Symmetry Search. *arXiv* **2018**, 1808.01590. https://arxiv.org/abs/1808.01590 (accessed Aug 11, 2021).
(96) Ong, S. P.; Richards, W. D.; Jain, A.; Hautier, G.; Kocher, M.; Cholia, S.; Gunter, D.; Chevrier, V. L.; Persson, K. A.; Ceder, G. Python Materials Genomics (Pymatgen): A Robust, Open-Source Python Library for Materials Analysis. *Comput. Mater. Sci.* **2013**, *68*, 314−319.
(97) Ong, S. P.; Wang, L.; Kang, B.; Ceder, G. Li-Fe-P-O_2 Phase Diagram from First Principles Calculations. *Chem. Mater.* **2008**, *20* (5), 1798−1807.
(98) Ong, S. P.; Jain, A.; Hautier, G.; Kang, B.; Ceder, G. Thermal Stabilities of Delithiated Olivine MPO_4 (M = Fe, Mn) Cathodes Investigated Using First Principles Calculations. *Electrochem. Commun.* **2010**, *12* (3), 427−430.
(99) Watson, S. C.; Carter, E. A. Spin-Dependent Pseudopotentials. *Phys. Rev. B: Condens. Matter Mater. Phys.* **1998**, *58* (20), R13309−R13313.
(100) Cocula, V.; Carter, E. A. Breakdown of the Pseudopotential Approximation for Magnetic Systems: Predicting Magnetic Quenching at the V(001) Surface with Spin-Dependent Pseudopotentials. *Phys. Rev. B: Condens. Matter Mater. Phys.* **2004**, *69* (5), 052404.
(101) Cocula, V.; Pickard, C. J.; Carter, E. A. Ultrasoft Spin-Dependent Pseudopotentials. *J. Chem. Phys.* **2005**, *123* (21), 214101.
(102) Cocula, V.; Starrost, F.; Watson, S. C.; Carter, E. A. Spin-Dependent Pseudopotentials in the Solid-State Environment: Applications to Ferromagnetic and Antiferromagnetic Metals. *J. Chem. Phys.* **2003**, *119* (15), 7659−7671.
(103) Starrost, F.; Kim, H.; Watson, S. C.; Kaxiras, E.; Carter, E. A. Density-Functional Theory Modeling of Bulk Magnetism with Spin-Dependent Pseudopotentials. *Phys. Rev. B: Condens. Matter Mater. Phys.* **2001**, *64* (23), 235105.
(104) Pedregosa, F.; Varoquaux, G.; Gramfort, A.; Michel, V.; Thirion, B.; Grisel, O.; Blondel, M.; Prettenhofer, P.; Weiss, R.; Dubourg, V.; Vanderplas, J.; Passos, A.; Cournapeau, D.; Brucher, M.; Perrot, M.; Duchesnay, É. Scikit-Learn: Machine Learning in Python. *J. Mach. Learn. Res.* **2011**, *12*, 2825−2830.
(105) Weng, B.; Song, Z.; Zhu, R.; Yan, Q.; Sun, Q.; Grice, C. G.; Yan, Y.; Yin, W.-J. Simple Descriptor Derived from Symbolic Regression Accelerating the Discovery of New Perovskite Catalysts. *Nat. Commun.* **2020**, *11* (1), 3513.
(106) Vaníysek, P.; Cheng, J.-P. *CRC Handbook of Chemistry and Physics*, 100th ed.; Rumble, J. R., Ed.; CRC Press: 2019.
(107) Kubaschewski, O.; Alcock, C. B. *Metallurgical Thermochemistry*, 5th ed.; Raynor, G. V., Ed.; Pergamon Press: 1979.
(108) Barin, I. *Thermochemical Data of Pure Substances*, 3rd ed.; Platzki, G., Ed.; VCH: 1995.
(109) Wagman, D. D.; Evans, W. H.; Parker, V. B.; Schumm, R. H.; Halow, I.; Bailey, S. M.; Churney, K. L.; Nuttall, R. L. Erratum: The NBS Tables of Chemical Thermodynamic Properties. Selected Values for Inorganic and C_1 and C_2 Organic Substances in SI Units [*J. Phys. Chem. Ref. Data 11*, Suppl. 2 (1982)]; Lide, D. R., Ed.; American Chemical Society: Washington, DC, 1989; Vol. *18*. DOI: 10.1063/1.555845.
(110) Chase, M. W., Jr.; Davies, C. A.; Downey, J. R., Jr.; Frurip, D. J.; McDonald, R. A.; Syverud, A. N. *NIST-JANAF Thermochemical Tables*, 4th ed.; National Institute of Standards and Technology: 1998.
(111) Watson, A.; Markus, T. *Ternary Steel Systems: Phase Diagrams and Phase Transition Data*; Springer: 2015.
(112) Kittel, C. *Introduction to Solid State Physics*, 8th ed.; Wiley: 2004.
(113) Jain, A.; Ong, S. P.; Hautier, G.; Chen, W.; Richards, W. D.; Dacek, S.; Cholia, S.; Gunter, D.; Skinner, D.; Ceder, G.; Persson, K. A. Commentary: The Materials Project: A Materials Genome Approach to Accelerating Materials Innovation. *APL Mater.* **2013**, *1* (1), 011002.
(114) Saal, J. E.; Kirklin, S.; Aykol, M.; Meredig, B.; Wolverton, C. Materials Design and Discovery with High-Throughput Density Functional Theory: The Open Quantum Materials Database (OQMD). *JOM* **2013**, *65* (11), 1501−1509.
(115) Kirklin, S.; Saal, J. E.; Meredig, B.; Thompson, A.; Doak, J. W.; Aykol, M.; Rühl, S.; Wolverton, C. The Open Quantum Materials Database (OQMD): Assessing the Accuracy of DFT Formation Energies. *npj Comput. Mater.* **2015**, *1* (1), 15010.
(116) Curtarolo, S.; Setyawan, W.; Hart, G. L. W.; Jahnatek, M.; Chepulskii, R. V.; Taylor, R. H.; Wang, S.; Xue, J.; Yang, K.; Levy, O.; Mehl, M. J.; Stokes, H. T.; Demchenko, D. O.; Morgan, D. AFLOW: An Automatic Framework for High-Throughput Materials Discovery. *Comput. Mater. Sci.* **2012**, *58*, 218−226.
(117) Sansonetti, J. E.; Martin, W. C.; Young, S. L. Handbook of Basic Atomic Spectroscopic Data http://physics.nist.gov/Handbook (accessed Jan 18, 2021). DOI: 10.18434/T4FW23.
(118) Carter, E. A.; Goddard, W. A., III Early- versus Late-Transition-Metal-Oxo Bonds: The Electronic Structure of Oxovanadium(1+) and Oxoruthenium(1+). *J. Phys. Chem.* **1988**, *92* (8), 2109−2115.
(119) Barcellos, D. R.; Sanders, M. D.; Tong, J.; McDaniel, A. H.; O'Hayre, R. P. $BaCe_{0.25}Mn_{0.75}O_{3-\delta}$ — a Promising Perovskite-Type Oxide for Solar Thermochemical Hydrogen Production. *Energy Environ. Sci.* **2018**, *11* (11), 3256−3265.
(120) Niazi, A.; Bud'ko, S. L.; Schlagel, D. L.; Yan, J. Q.; Lograsso, T. A.; Kreyssig, A.; Das, S.; Nandi, S.; Goldman, A. I.; Honecker, A.; McCallum, R. W.; Reehuis, M.; Pieper, O.; Lake, B.; Johnston, D. C. Single-Crystal Growth, Crystallography, Magnetic Susceptibility, Heat Capacity, and Thermal Expansion of the Antiferromagnetic S = 1 Chain Compound CaV_2O_4. *Phys. Rev. B: Condens. Matter Mater. Phys.* **2009**, *79* (10), 104432.
(121) Li, X.; Buttrey, D. J.; Blom, D. A.; Vogt, T. Improvement of the Structural Model for the M1 Phase Mo-V-Nb-Te-O Propane (Amm)Oxidation Catalyst. *Top. Catal.* **2011**, *54* (10−12), 614−626.
(122) Joshi, R.; Kumar, P.; Gaur, A.; Asokan, K. Structural, Optical and Ferroelectric Properties of V Doped ZnO. *Appl. Nanosci.* **2014**, *4* (5), 531−536.
(123) Greenwood, N. N.; Earnshaw, A. *Chemistry of the Elements*; Elsevier: 2012.
(124) Bartel, C. J.; Sutton, C.; Goldsmith, B. R.; Ouyang, R.; Musgrave, C. B.; Ghiringhelli, L. M.; Scheffler, M. New Tolerance Factor to Predict the Stability of Perovskite Oxides and Halides. *Sci. Adv.* **2019**, *5* (2), No. eaav0693.
(125) Silva, J.; Reyes, A.; Esparza, H.; Camacho, H.; Fuentes, L. $BiFeO_3$: A Review on Synthesis, Doping and Crystal Structure. *Integr. Ferroelectr.* **2011**, *126* (1), 47−59.

(126) Azuma, M.; Niitaka, S.; Hayashi, N.; Oka, K.; Takano, M.; Funakubo, H.; Shimakawa, Y. Rhombohedral-Tetragonal Phase Boundary with High Curie Temperature in (1-x)$BiCoO_{3-x}BiFeO_3$ Solid Solution. *Jpn. J. Appl. Phys.* **2008**, *47* (9), 7579−7581.
(127) Yi, H. T.; Choi, T.; Choi, S. G.; Oh, Y. S.; Cheong, S.-W. Mechanism of the Switchable Photovoltaic Effect in Ferroelectric $BiFeO_3$. *Adv. Mater.* **2011**, *23* (30), 3403−3407.
(128) Haertling, G. H. Ferroelectric Ceramics: History and Technology. In *Ferroelectricity*; Wiley-VCH: 2007; Vol. *818*, pp 157−178. DOI: 10.1002/9783527618002.ch6.
(129) Shukla, R.; Bera, A. K.; Yusuf, S. M.; Deshpande, S. K.; Tyagi, A. K.; Hermes, W.; Eul, M.; Pöttgen, R. Multifunctional Nanocrystalline $CeCrO_3$: Antiferromagnetic, Relaxor, and Optical Properties. *J. Phys. Chem. C* **2009**, *113* (29), 12663−12668.
(130) Cai, T.-Y.; Liu, S.-C.; Ju, S.; Liu, C.-Y.; Guo, G.-Y. Multiferroic Double Perovskites $ScFe_{1-x}Cr_xO_3$ $(1/6 \leq x \leq 5/6)$ for Highly Efficient Photovoltaics and Spintronics. *Phys. Rev. Appl.* **2017**, *8* (3), 034034.
(131) Tang, P.; Chen, H.; Cao, F.; Pan, G. Magnetically Recoverable and Visible-Light-Driven Nanocrystalline $YFeO_3$ Photocatalysts. *Catal. Sci. Technol.* **2011**, *1* (7), 1145.
(132) Shen, H.; Xu, J.; Wu, A.; Zhao, J.; Shi, M. Magnetic and Thermal Properties of Perovskite $YFeO_3$ Single Crystals. *Mater. Sci. Eng., B* **2009**, *157* (1−3), 77−80.
(133) Varignon, J.; Bibes, M.; Zunger, A. Mott Gapping in 3d ABO_3 Perovskites without Mott-Hubbard Interelectronic Repulsion Energy U. *Phys. Rev. B: Condens. Matter Mater. Phys.* **2019**, *100* (3), 035119.
(134) Gao, F.; Yuan, Y.; Wang, K. F.; Chen, X. Y.; Chen, F.; Liu, J.-M.; Ren, Z. F. Preparation and Photoabsorption Characterization of $BiFeO_3$ Nanowires. *Appl. Phys. Lett.* **2006**, *89* (10), 102506.
(135) Scott, J. F.; Palai, R.; Kumar, A.; Singh, M. K.; Murari, N. M.; Karan, N. K.; Katiyar, R. S. New Phase Transitions in Perovskite Oxides: $BiFeO_3$, $SrSnO_3$, and $Pb(Fe_{2/3}W_{1/3})_{1/2}Ti_{1/2}O_3$. *J. Am. Ceram. Soc.* **2008**, *91* (6), 1762−1768.
(136) McLeod, J. A.; Pchelkina, Z. V.; Finkelstein, L. D.; Kurmaev, E. Z.; Wilks, R. G.; Moewes, A.; Solovyev, I. V.; Belik, A. A.; Takayama-Muromachi, E. Electronic Structure of $BiMO_3$ Multiferroics and Related Oxides. *Phys. Rev. B: Condens. Matter Mater. Phys.* **2010**, *81* (14), 144103.
(137) Setyawan, W.; Curtarolo, S. High-Throughput Electronic Band Structure Calculations: Challenges and Tools. *Comput. Mater. Sci.* **2010**, *49* (2), 299−312.
(138) Stevanović, V.; Lany, S.; Zhang, X.; Zunger, A. Correcting Density Functional Theory for Accurate Predictions of Compound Enthalpies of Formation: Fitted Elemental-Phase Reference Energies. *Phys. Rev. B: Condens. Matter Mater. Phys.* **2012**, *85* (11), 115104.
(139) Lany, S. Band-Structure Calculations for the 3d Transition Metal Oxides in GW. *Phys. Rev. B: Condens. Matter Mater. Phys.* **2013**, *87* (8), 085112.
(140) Lany, S. Semiconducting Transition Metal Oxides. *J. Phys.: Condens. Matter* **2015**, *27* (28), 283203.
(141) Kübler, J. *Theory of Itinerant Electron Magnetism*; Oxford University Press: 2017.
(142) Laursen, A. B.; Wexler, R. B.; Whitaker, M. J.; Izett, E. J.; Calvinho, K. U. D.; Hwang, S.; Rucker, R.; Wang, H.; Li, J.; Garfunkel, E.; Greenblatt, M.; Rappe, A. M.; Dismukes, G. C. Climbing the Volcano of Electrocatalytic Activity While Avoiding Catalyst Corrosion: Ni_3P, a Hydrogen Evolution Electrocatalyst Stable in Both Acid and Alkali. *ACS Catal.* **2018**, *8* (5), 4408−4419.
(143) Kibsgaard, J.; Tsai, C.; Chan, K.; Benck, J. D.; Nørskov, J. K.; Abild-Pedersen, F.; Jaramillo, T. F. Designing an Improved Transition Metal Phosphide Catalyst for Hydrogen Evolution Using Experimental and Theoretical Trends. *Energy Environ. Sci.* **2015**, *8* (10), 3022−3029.
(144) Liu, P.; Rodriguez, J. A. Catalysts for Hydrogen Evolution from the [NiFe] Hydrogenase to the $Ni_2P(001)$ Surface: The Importance of Ensemble Effect. *J. Am. Chem. Soc.* **2005**, *127* (42), 14871−14878.
(145) Wagner, S.; Shay, J. L.; Migliorato, P.; Kasper, H. M. $CuInSe_2/CdS$ Heterojunction Photovoltaic Detectors. *Appl. Phys. Lett.* **1974**, *25* (8), 434−435.
(146) Chen, S.; Walsh, A.; Gong, X.-G.; Wei, S.-H. Classification of Lattice Defects in the Kesterite Cu_2ZnSnS_4 and $Cu_2ZnSnSe_4$ Earth-Abundant Solar Cell Absorbers. *Adv. Mater.* **2013**, *25* (11), 1522−1539.
(147) Wexler, R. B.; Gautam, G. S.; Carter, E. A. Optimizing Kesterite Solar Cells from Cu_2ZnSnS_4 to $Cu_2CdGe(S,Se)_4$. *J. Mater. Chem. A* **2021**, *9* (15), 9882−9897.
(148) Kakekhani, A.; Katti, R. N.; Rappe, A. M. Water in Hybrid Perovskites: Bulk $MAPbI_3$ Degradation via Super-Hydrous State. *APL Mater.* **2019**, *7* (4), 041112.
(149) Kim, Y.-H.; Kim, S.; Kakekhani, A.; Park, J.; Park, J.; Lee, Y.-H.; Xu, H.; Nagane, S.; Wexler, R. B.; Kim, D.-H.; Jo, S. H.; Martínez-Sarti, L.; Tan, P.; Sadhanala, A.; Park, G.-S.; Kim, Y.-W.; Hu, B.; Bolink, H. J.; Yoo, S.; Friend, R. H.; Rappe, A. M.; Lee, T.-W. Comprehensive Defect Suppression in Perovskite Nanocrystals for High-Efficiency Light-Emitting Diodes. *Nat. Photonics* **2021**, *15* (2), 148−155.
(150) Burschka, J.; Pellet, N.; Moon, S.-J.; Humphry-Baker, R.; Gao, P.; Nazeeruddin, M. K.; Grätzel, M. Sequential Deposition as a Route to High-Performance Perovskite-Sensitized Solar Cells. *Nature* **2013**, *499* (7458), 316−319.
(151) Ritzmann, A. M.; Muñoz-García, A. B.; Pavone, M.; Keith, J. A.; Carter, E. A. Ab Initio Evaluation of Oxygen Diffusivity in $LaFeO_3$: The Role of Lanthanum Vacancies. *MRS Commun.* **2013**, *3* (3), 161−166.
(152) Chen, S.; Yang, J. H.; Gong, X. G.; Walsh, A.; Wei, S.-H. Intrinsic Point Defects and Complexes in the Quaternary Kesterite Semiconductor Cu_2ZnSnS_4. *Phys. Rev. B: Condens. Matter Mater. Phys.* **2010**, *81* (24), 35−37.
(153) Yin, W.-J.; Wei, S.-H.; Al-Jassim, M. M.; Yan, Y. Origin of the Diverse Behavior of Oxygen Vacancies in ABO_3 Perovskites: A Symmetry Based Analysis. *Phys. Rev. B: Condens. Matter Mater. Phys.* **2012**, *85* (20), 201201.
(154) Wexler, R. B.; Sohlberg, K. Role of Proton Hopping in Surface Charge Transport on Tin Dioxide as Revealed by the Thermal Dependence of Conductance. *J. Phys. Chem. A* **2014**, *118* (51), 12031−12040.